Joule

CellPress

Article

Sulfur-Modulated Tin Sites Enable Highly Selective Electrochemical Reduction of CO_2 to Formate

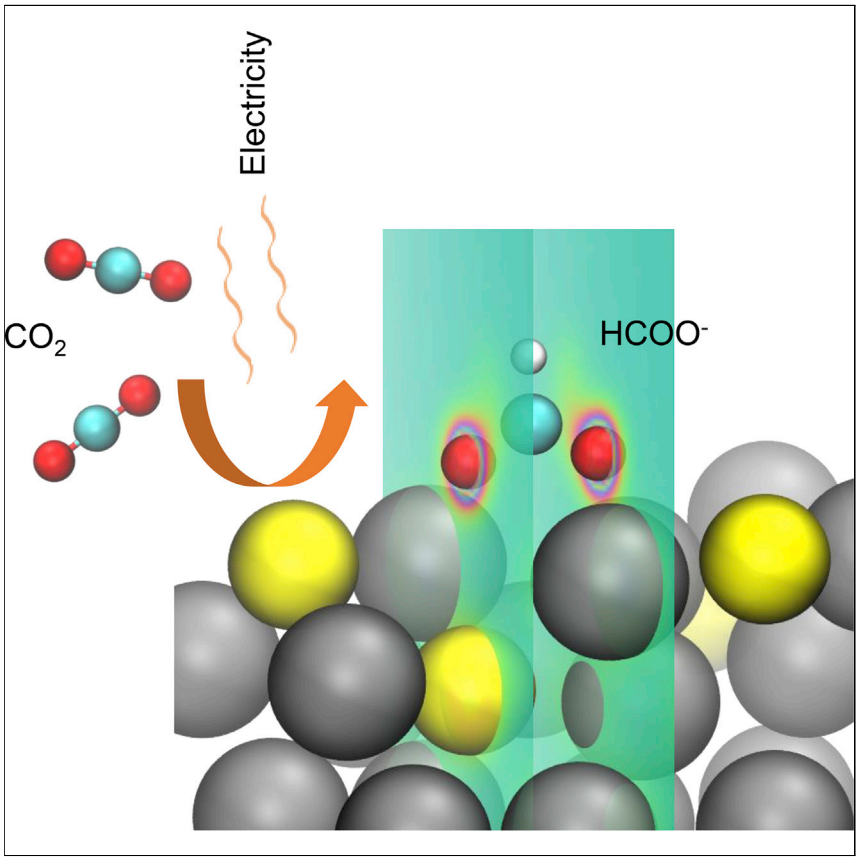

The electrochemical reduction of carbon dioxide (CO_2RR) offers a compelling route to energy storage and high-value chemical manufacture. The presence of sulfur atoms in catalyst surfaces promotes undercoordinated sites, thereby improving the electrochemical reduction of CO_2 to formate. The resulting sulfur-modulated tin catalysts accelerate CO_2RR at geometric current densities of 55 mA cm^{-2} at −0.75 V versus RHE with a Faradaic efficiency of 93%.

Xueli Zheng, Phil De Luna, F. Pelayo García de Arquer, ..., Xiwen Du, Peidong Yang, Edward H. Sargent

ted.sargent@utoronto.ca

HIGHLIGHTS

Electrochemical reduction of CO_2 to renewable fuels is urgently needed

The incorporation of sulfur into tin favors formate generation

Sulfur-modulated tin increases the CO_2 reduction current density

Sulfur-modulated tin provides excellent stability

Zheng et al., Joule 1, 794–805
December 20, 2017
https://doi.org/10.1016/j.joule.2017.09.014

Joule

CellPress

Article

Sulfur-Modulated Tin Sites Enable Highly Selective Electrochemical Reduction of CO_2 to Formate

Xueli Zheng,[1,2,6,9] Phil De Luna,[3,4,9] F. Pelayo García de Arquer,[1] Bo Zhang,[1] Nigel Becknell,[4] Michael B. Ross,[4] Yifan Li,[4,7] Mohammad Norouzi Banis,[5] Yuzhang Li,[6] Min Liu,[1] Oleksandr Voznyy,[1] Cao Thang Dinh,[1] Taotao Zhuang,[1] Philipp Stadler,[8] Yi Cui,[6] Xiwen Du,[2] Peidong Yang,[4,7] and Edward H. Sargent[1,10,*]

SUMMARY

Electrochemical reduction of carbon dioxide (CO_2RR) to formate provides an avenue to the synthesis of value-added carbon-based fuels and feedstocks powered using renewable electricity. Here, we hypothesized that the presence of sulfur atoms in the catalyst surface could promote undercoordinated sites, and thereby improve the electrochemical reduction of CO_2 to formate. We explored, using density functional theory, how the incorporation of sulfur into tin may favor formate generation. We used atomic layer deposition of SnS_x followed by a reduction process to synthesize sulfur-modulated tin (Sn(S)) catalysts. X-ray absorption near-edge structure (XANES) studies reveal higher oxidation states in Sn(S) compared with that of tin in Sn nanoparticles. Sn(S)/Au accelerates CO_2RR at geometric current densities of 55 mA cm^{-2} at −0.75 V versus reversible hydrogen electrode with a Faradaic efficiency of 93%. Furthermore, Sn(S) catalysts show excellent stability without deactivation (<2% productivity change) following more than 40 hours of operation.

INTRODUCTION

The electrochemical reduction of carbon dioxide (CO_2RR) offers a compelling route to energy storage and high-value chemical manufacture.[1–4] It enables the use of increasingly abundant renewable energy sources, such as solar and wind, to drive the conversion of CO_2 to renewable fuels and feedstocks. This approach stands to reduce present-day dependence on conventional fuels and also help mitigate net CO_2 emissions. Despite recent breakthroughs, the energy efficiency of CO_2RR is still far from being a viable alternative to fossil energy sources.[4–7] Improvements in selectivity and partial current density with robust and stable long operating times are of crucial importance to continue advances in the direction of commercial viability.

Formate is one interesting product among the variety that can be synthesized via CO_2RR. It can be directly used as a fuel, as a means of H_2 storage, or as a feedstock in the synthesis of fine chemicals of interest to the pharmaceutical industry.[8,9] A recent paper utilizing a gross-margin model for defining technoeconomic benchmarks for CO_2 reduction showed that formate and carbon monoxide may offer paths to economically viable products.[10] Unfortunately, in the case of formate, high selectivity has been achieved only at the expense of low current density, yielding

Context & Scale

With rapid advances in the efficient and cost-effective conversion of sunlight to electrical power, the development of storage technologies for renewable energy is even more urgent. Using renewable electricity to convert CO_2 into formate simultaneously addresses the need for storage of intermittent renewable energy sources and the need to reduce greenhouse gas emissions. We report an increase of greater than 4-fold in the current density (hence the rate of reaction) in formate electrosynthesis compared with relevant controls. Our catalysts also show excellent stability without deactivation (<2% productivity change) following more than 40 hours of operation.

impractically low partial current densities (j_{HCOO^-}). In addition, many catalysts exhibit rapid deactivation within hours.[4,11–15]

Metal surfaces have been widely used for the heterogeneous electroreduction of CO_2 due to their robustness and superior catalytic activity.[6,14,16] Different strategies have been explored to control selectivity, reduce overpotentials, and increase energy efficiency.[17–26] From a materials perspective, the choice of metals can be used to tailor CO_2RR selectivity. For example, metals such as Pd, Pb, Co, Hg, In, Bi, Cd, or Sn have been reported to favor selectivity toward formate over carbon monoxide or hydrogen.[4,13,17–24] On the other hand, it has been shown that the presence of high-index facets, undercoordinated sites, and adatoms can improve CO_2RR energetics as the energy required for the intermediate steps in the electroreduction of CO_2 is lowered.[25–27]

The use of metal-oxide-derived catalysts has been found to increase performance in CO_2 reduction when compared with their fully reduced counterparts.[4,12,21] Metal electrodes obtained from the reduction of metal oxides exhibit a prominent increase in selectivity and provide lower overpotentials in the electrosynthesis of CO and ethylene.[28] This is ascribed to a combination of an increased number of undercoordinated sites, the presence of oxygen promoters in metal oxides, and the synergetic effect between remaining oxide species and native metal atoms.[4,21,28]

Here, we demonstrate the use of sulfide-derived metal catalysts to promote a high number of favorable catalytic sites. We obtain, as a result, high selectivity and high partial current density for CO_2RR to formate. We hypothesized that sulfur-modulated tin catalysts (Sn(S)) could offer superior catalytic selectivity, since the removal of sulfur atoms incorporated in the Sn slab leads to a surface lattice distortion, thereby generating undercoordinated active Sn sites. We developed a materials strategy based on atomic layer deposition that combines ultra-sharp features—which enable exploitation of field-induced reagent concentration (FIRC)[3]—with the benefits of a tin sulfide-derived catalyst. As a result, we report high current density to geometric formate (~55 mA cm^{-2}). The new catalysts exhibit excellent stability over the course of a 40-hr initial study.

RESULTS AND DISCUSSION

Computational Studies

We first sought to model the effect on the catalytic activity of CO_2RR to formate provided by doping sulfur atoms into Sn slabs. To this end, we carried out a computational study in which we systematically varied the sulfur content from pure tin to tin(II) sulfide. Density functional theory (DFT) calculations were used to probe the energetics along the different CO_2RR pathways toward formate, carbon monoxide, and hydrogen. Different sulfur contents are expected to modify the surface morphology and electronic structure thereby affecting the CO_2RR activity (Figure S1). The electrochemical reduction of CO_2 to formate is known to proceed via an initial proton-coupled electron transfer to form a bound formate intermediate (HCOO*).[25] Other competing reaction pathways have different predominant intermediates. Carbon monoxide evolution, for example, typically proceeds via a bound carboxylate intermediate (COOH*).[3,29] The hydrogen evolution reaction (HER), on the other hand, requires a bound proton (H*) intermediate.[30]

A highly selective catalyst for the production of formic acid will favor the formation of formate over carboxylate and proton intermediates. To assess the selectivity and

[1]Department of Electrical and Computer Engineering, University of Toronto, 35 St George Street, Toronto, ON M5S 1A4, Canada

[2]Institute of New-Energy Materials, School of Materials Science and Engineering, Tianjin University, Tianjin 300072, China

[3]Department of Materials Science and Engineering, University of Toronto, 184 College Street, Toronto, ON M5S 3E4, Canada

[4]Department of Chemistry, University of California, Berkeley, Berkeley, CA 94720, USA

[5]Canadian Light Source, Inc.(CLSI), 44 Innovation Boulevard, Saskatoon, SK S7N 2V3, Canada

[6]Department of Material Science and Engineering, Stanford University, Stanford, CA 94305, USA

[7]Chemical Sciences Division, Lawrence Berkeley National Laboratory, Berkeley, CA 94720, USA

[8]Institute of Physical Chemistry, Johannes Kepler University Linz, Altenberger Strasse 69, 4040 Linz, Austria

[9]These authors contributed equally

[10]Lead contact

*Correspondence: ted.sargent@utoronto.ca

https://doi.org/10.1016/j.joule.2017.09.014

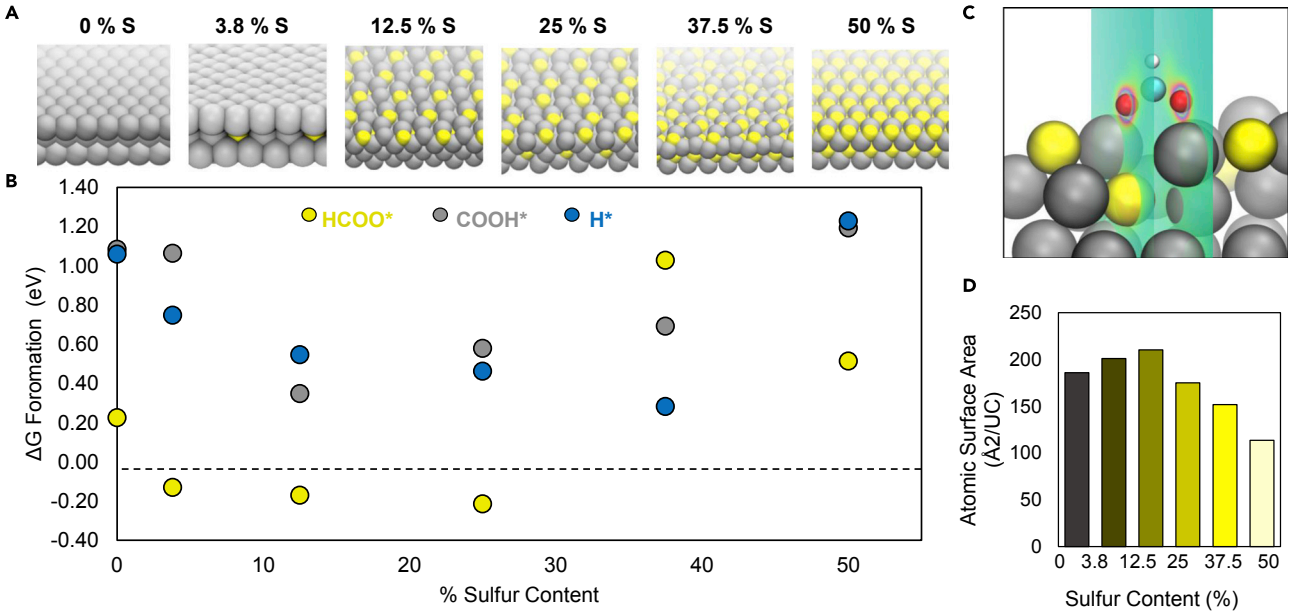

Figure 1. Computational Investigation of Sulfur-Modulated Tin System

(A) Optimized surface slab structures of pure Sn, S-modulated Sn, and SnS.

(B) Gibbs free energies of formation ($\Delta G_{formation}$) for HCOO* (yellow), COOH* (gray), and H* (blue) intermediates, which are the rate-limiting intermediates along the reaction pathway to produce formate, carbon monoxide, and hydrogen gas, respectively.

(C) Volume slice of the charge densities through the middle of the oxygen atom of a bound HCOO* intermediate.

(D) Atomic accessible surface area of the metal slab normalized to the number of tin atoms as a function of sulfur content.

limiting potentials for each product, we calculated the Gibbs free energy of formation (ΔG_f) for HCOO*, COOH*, and H* intermediates on the (100) surface of Sn(S) as a function of sulfur content (Figure 1B and Table S3). The bound HCOO* intermediate visualized with a volume slice of the electronic charge densities through the center of the oxygen atoms is shown in Figure 1C. Here, the free energy of formation is the reaction free energy necessary to electrochemically reduce CO_2 to a surface intermediate species at 0 V versus reversible hydrogen electrode (RHE) at pH 0, 298 K, and 1 atm. In the majority of cases, the Gibbs free energy of formation for HCOO* is lower than that of COOH*. This suggests that the production of formic acid is the energetically preferred pathway. The reaction energy diagram for electroreduction of CO_2 to formic acid with catalysts of various sulfur content is shown in Figure S2. For both formate and carboxylate intermediates, the same trend is observed whereby a slight doping of S into Sn drastically lowers ΔG_f and, as the content of S increases, so does the free energy of formation. An opposite trend was observed for H*, whereby the free energy of formation increases upon S incorporation.

Interestingly, the ΔG_f for HCOO* was found to be negative for 3.8% (−0.13 eV), 12.5% (−0.17 eV), and 25% (−0.21 eV) S-doped Sn. This suggests that the formation of the rate-limiting formate intermediate is thermodynamically downhill when sulfur is slightly doped into tin.

The theoretical limiting potential for CO_2RR—the calculated minimum thermodynamic potential necessary to drive the electrochemical reaction forward—was found to be closest to zero for 3.8% S with a value of −0.07 V versus RHE at pH 0, 298 K, and 1 atm (Table S4). The limiting potential is taken from the reaction energy diagram (Figure S2) and is the largest ΔG along the reaction pathway. For this same composition, the limiting potentials for CO production and HER were much more negative

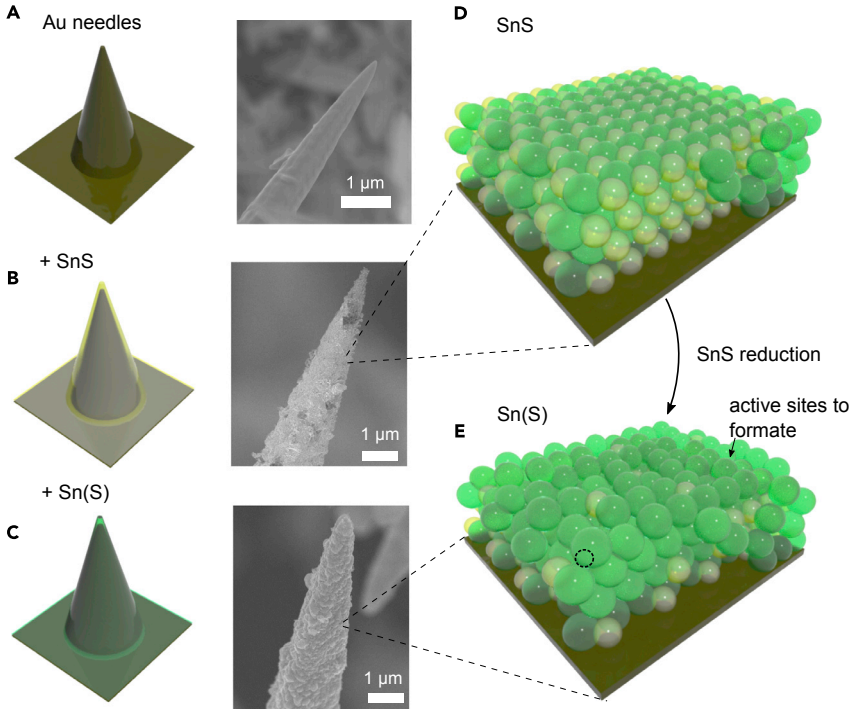

Figure 2. Fabrication of Nanostructured Sn(S) Catalysts

(A–C) Schematic and SEM images of the process leading to the fabrication of Sn(S) nanostructured electrodes. (A) Au needles. (B) Au needles after SnS deposition by ALD process. (C) Au needles coated with sulfur-modulated-tin films.

(D) A SnS_x slab is conformally deposited by ALD on top of the nanostructured metal backbone.

(E) The selective reduction of SnS_x leads to Sn(S) films, which promotes CO_2RR toward formate. The dashed circle means active sites for formate generation.

(−1.06 V and −0.75 V, respectively). These results suggest that the onset potential for formate production may be lower than that of CO or H_2, highlighting the beneficial effects of S incorporation on the energetics of formate generation.

To computationally investigate the morphological changes that doping induced on the tin, accessible surface areas were calculated using Connolly surface areas (Figure S3 and Table S6). It was found that slight doping of sulfur atoms increased the atomic surface area (normalized to the number of tin atoms in the slab) compared with tin sulfide or pure tin by 13% (Figure 1D). The 12.5% sulfur-doped Sn(S) structure had the largest accessible surface area of 210 $Å^2$ per unit cell, whereas the close-packed pure tin structure had the lowest accessible surface area of 186 $Å^2$ per unit cell. This high surface area suggests the surface has a greater degree of accessibility and is more likely to have undercoordinated sites due to the imperfect packing caused by the slight doping of sulfur. This result was validated by comparing the electrochemically active surface area (ECSA) of Sn(S) and Sn nanoparticles (NPs) as described later in the text.

Synthesis and Characterization of Sulfur-Modulated Tin Catalysts

A method to achieve a controllably sulfur-doped Sn surface was then required to successfully implement these findings. We took the view that atomic layer deposition (ALD) could provide precise control over both S content and film thickness (Figures 2 and S4). SnS_x thin films were deposited from the reaction of tetrakis(dimethylamino)tin(IV) (TDMA-Sn) and H_2S. The resulting films were then electrochemically

Table 1. Comparison of Catalytic Parameters of Sulfur-Modulated Tin Catalysts and Controls

Samples	Electrolyte	Potential (V versus RHE)	Current Density (mA cm^{-2})	Faradaic Efficiency (%)	Reference
Sn(S)/Au	0.1 M $KHCO_3$	−0.75	55	93.3	This work
Sn nanoparticles/Au	0.1 $MKHCO_3$	−0.75	42	30.2	This work
SnO_x-derived Sn	0.5 M $KHCO_3$	−1.05	12	19	Lu et al.[11]
SnO_2 nanoparticles	0.1 M $KHCO_3$	−1.05	9.5	90	Kim et al.[14]
SnO_x/Sn	0.1 M $KHCO_3$	−1.05	11	70	Pander et al.[22]
Oxide-derived Pb	0.5 M $KHCO_3$	−1.05	1	95	Hollingsworth et al.[23]
SnS_2-derived Sn/rGO	0.5 M $KHCO_3$	−1.05	11.75	85	Li et al.[31]
Sn quantum sheets/GO	0.1 M $KHCO_3$	−1.05	12	60	Lei et al.[32]
Partial oxidized Co	0.1 M Na_2SO_4	−0.24	10	90	Gao et al.[4]
Pd nanoparticles	0.5 M $KHCO_3$	−0.20	22	97	Klinkova et al.[13]
Pd nanoparticles	0.5 M $KHCO_3$	−0.35	8	90	Won da et al.[18]
Sn	$[Bmim]PF_6$	−1.05	15	95	Lee et al.[16]

reduced to partially remove S atoms (see Experimental Procedures for details), thereby increasing the density of active sites. *In situ* Raman spectra at −1.0 V versus RHE confirmed that the bulk and vast majority of SnS_x is reduced to Sn metal at high potentials (Figure S5). As discussed later, the catalytic activity of Sn(S)/Au shows significantly superior performance than pure Sn nanoparticles/Au samples, which is in agreement with DFT calculations (Table 1).

Morphological strategies have been shown to dramatically increase the rate for CO_2RR toward a given product. Field-induced reagent concentration (FIRC) is a catalytic phenomenon that was first reported on nanostructured gold nanoneedles for the reduction of CO_2 to CO (Figure 2A).[3] Simply, high-curvature nanostructures exhibit a high local negative electric field, which concentrates proximate positively charged cations that help to stabilize CO_2 reduction intermediates, promoting CO_2RR. Computational studies have since shown that strong local electric fields and the presence of cations proximate to the surface promote CO_2RR.[33] The concept of sharp nanostructures promoting CO_2RR activity and boosting current densities has since been demonstrated for CO_2 reduction to formate[13] and formic acid oxidation[15] on branched Pd NPs and CO_2 reduction to ethylene on copper nanodendrites.[17]

We sought to explore the synergy between FIRC and sulfur-modulated tin catalysts, building hybrid electrodes that combine the best nanostructured FIRC morphologies of Au nanoneedles with Sn(S), which improves formate evolution energetics (Figure 2). This required that the sulfur-modulated tin film be conformally deposited over the Au nanoneedles, maximizing activity toward the desired products and otherwise blocking CO active Au facets. We optimized the ALD process by controlling substrate preparation, pulse duration, and the number of cycles (Figures 2B and 2D). We achieved homogeneously dispersed sulfur elements into the Sn metal by ALD of SnS_x followed by an *in situ* reduction process to give the active Sn(S) catalyst (Figures 2C and 2E). We have found that regardless of starting Sn:S composition (1:1 or 1:2), the majority of the sulfur is removed during the reduction step. These results imply a limitation to the amount of sulfur that can remain after the initial reduction to SnS_x (Figure S13).

High-resolution transmission electron microscopy (HRTEM) studies were performed to provide greater insight into the surface structure and morphology of the catalyst

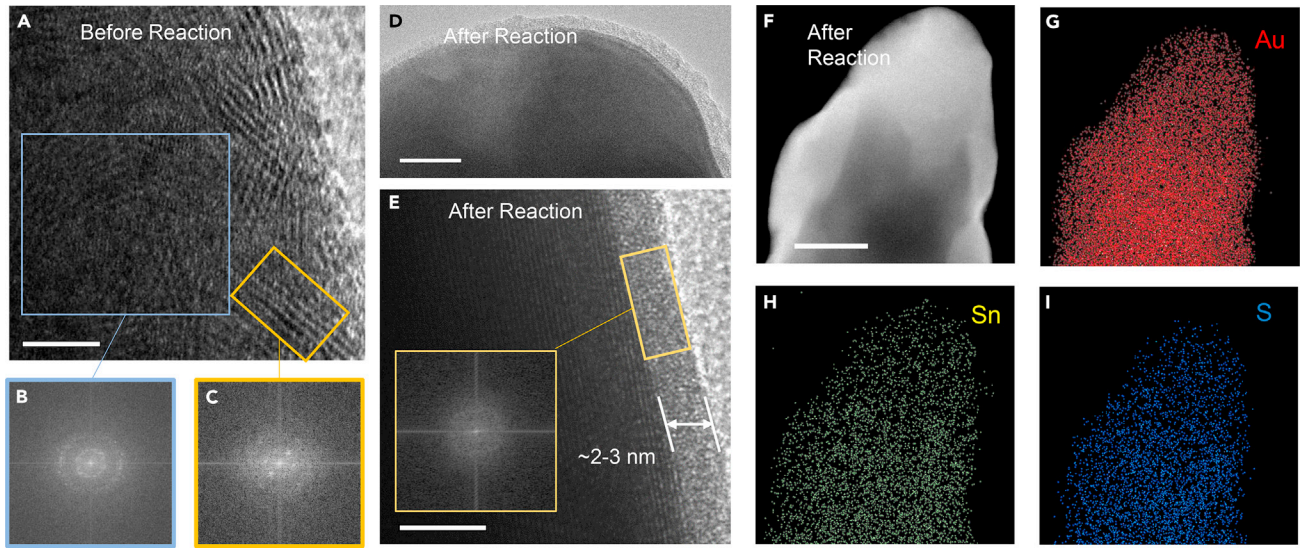

Figure 3. Characterization of Sulfur-Modulated Tin Catalysts

(A) High-resolution transmission electron microscope (HRTEM) image of the ALD SnS_x before reaction showing a highly polycrystalline surface. Scale bar represents 5 nm.

(B and C) Fast Fourier transform (FFT) of the polycrystalline region (B) and one specific crystalline grain (C).

(D and E) HRTEM image of the reduced Sn(S) active catalyst after reaction showing a uniform amorphous layer on the surface. Scale bar represents 20 nm for (D); scale bar represents 5 nm for (E). Inset is the FFT of the amorphous region.

(F–I) STEM image (F) of Sn(S)/Au and the corresponding EDS mapping to show homogeneously dispersed Au (G), Sn (H), and S (I). Scale bar represents 100 nm.

before and after reaction (Figure 3). It was found that, before reaction, highly polycrystalline tin sulfide is formed with extremely small grain sizes of ~5 nm (Figures 3A–3C). After reaction, a thin layer of amorphous tin-based material about 2–3 nm thick forms on the surface (Figures 3D and 3E). Scanning transmission electron microscopy-energy dispersive spectroscopy (STEM-EDS) elemental mapping showed a conformal coating of Sn(S) on Au needles, and a uniform, uncorrelated spatial distribution of Au, Sn, and S (Figures 3F–3I), consistent with the EDS line scan (Figure S6).

To elucidate the electronic configuration of the resulting Sn(S) layer in the final structure, we performed X-ray absorption spectroscopy (XAS) on Sn(S) and Sn NPs before, *in situ*, and after reaction (Figure 4). Sn NPs were used as a control of Sn(S). We analyzed the edge position of each compound as it shifts to higher energies with increasing oxidation of Sn.[34,35] *In situ* Sn L_3-edge spectra at −0.7 V versus RHE indicate that the reduction of SnS_x to Sn(S) resulted in an oxidation state between Sn^0 and Sn^{2+}, while Sn NPs do not change oxidation state (Figure 4A).[36,37] This suggests Sn(S) at −0.7 V versus RHE was more oxidized than Sn metal, which agreed with the *in situ* S K-edge spectra[38] (Figure S11). The trend observed from the Sn L_3-edge (Figure 4B) indicates that sulfur-doped Sn possessed a higher oxidation state than Sn NPs after reaction (edge shift indicated by a red arrow),[36,37] consistent with Sn K-edge measurements (Figure 4C).[35] Sn(S) exhibited a higher oxidation state than Sn NPs after reaction because Sn(S) was more readily oxidized to high valence after exposure to the open circuit potential and air. We propose that Sn(S) may have more undercoordinated Sn sites than the Sn NP control.

The surface chemical compositions of SnS_x, Sn(S) after reaction, and Sn NPs after reaction were further probed by X-ray photoelectron spectroscopy (XPS). The S 2p spectra of Sn(S) after reaction revealed the survival of sulfur throughout the reaction (Figure 4D). Based on the results from XPS analysis, the content of S in the Sn(S)

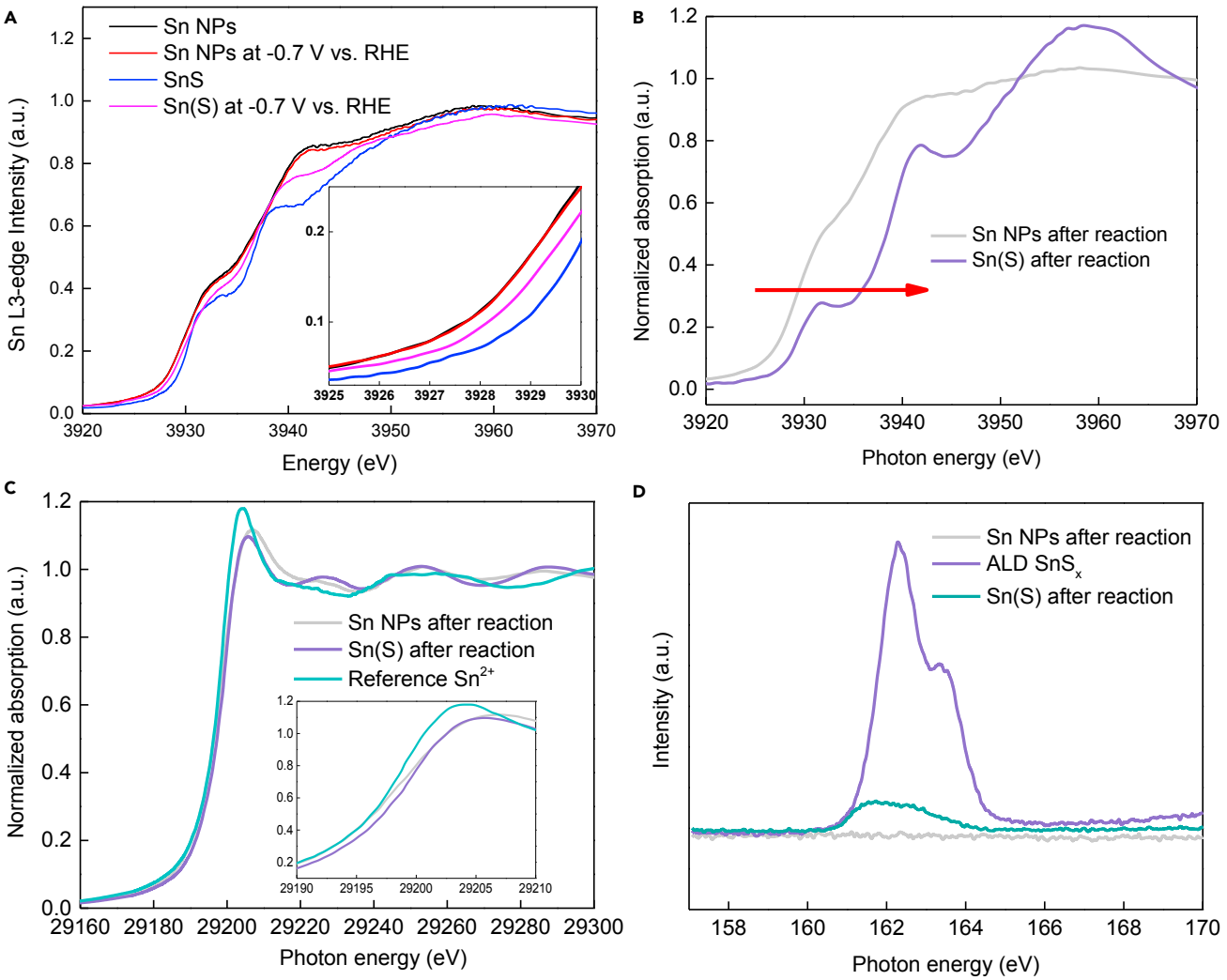

Figure 4. Electronic Structure of Sn(S) and Sn

(A) *In situ* Sn L_3-edge XANES spectra of Sn NPs, SnS, Sn NPs at −0.7 V versus RHE, and Sn(S) at −0.7 V versus RHE. Inset shows zoom in of the pre-edge energy range.

(B) Sn L_3-edge spectra of Sn(S) and Sn NPs on carbon paper after reaction (edge shift indicated by a red arrow).

(C) Sn K-edge of Sn(S) and relevant controls. Inset shows zoom in of the pre-edge energy range.

(D) XPS spectra of Sn(S), Sn NPs, and ALD SnS_x.

catalyst was calculated to be 3.2%. To avoid the effect of Au substrates and thus the potential increased sulfur content adhering to gold, we deposited Sn(S) on carbon paper (Figure S14) and found the content of S in the Sn(S)/carbon paper after reaction to be 4.6% (Figure S15).

Evaluation of Activity for Electrochemical Reduction of CO_2

We then proceeded to evaluate the catalytic performance of the Sn(S)-FIRC hybrid electrodes. Linear sweep voltammetry traces reveal the superior current density of S-modulated Sn samples over bare Sn NPs (Figure 5A). The Faradaic efficiency of S-modulated Sn samples approaches 100% for potentials more negative than −600 mV versus RHE. The resulting partial current density is significantly higher than that of Sn samples (Figures 5B and S12). We have also synthesized Sn film on Au needles by sputtering as a control (Figure S19). A record Faradaic efficiency of 93%

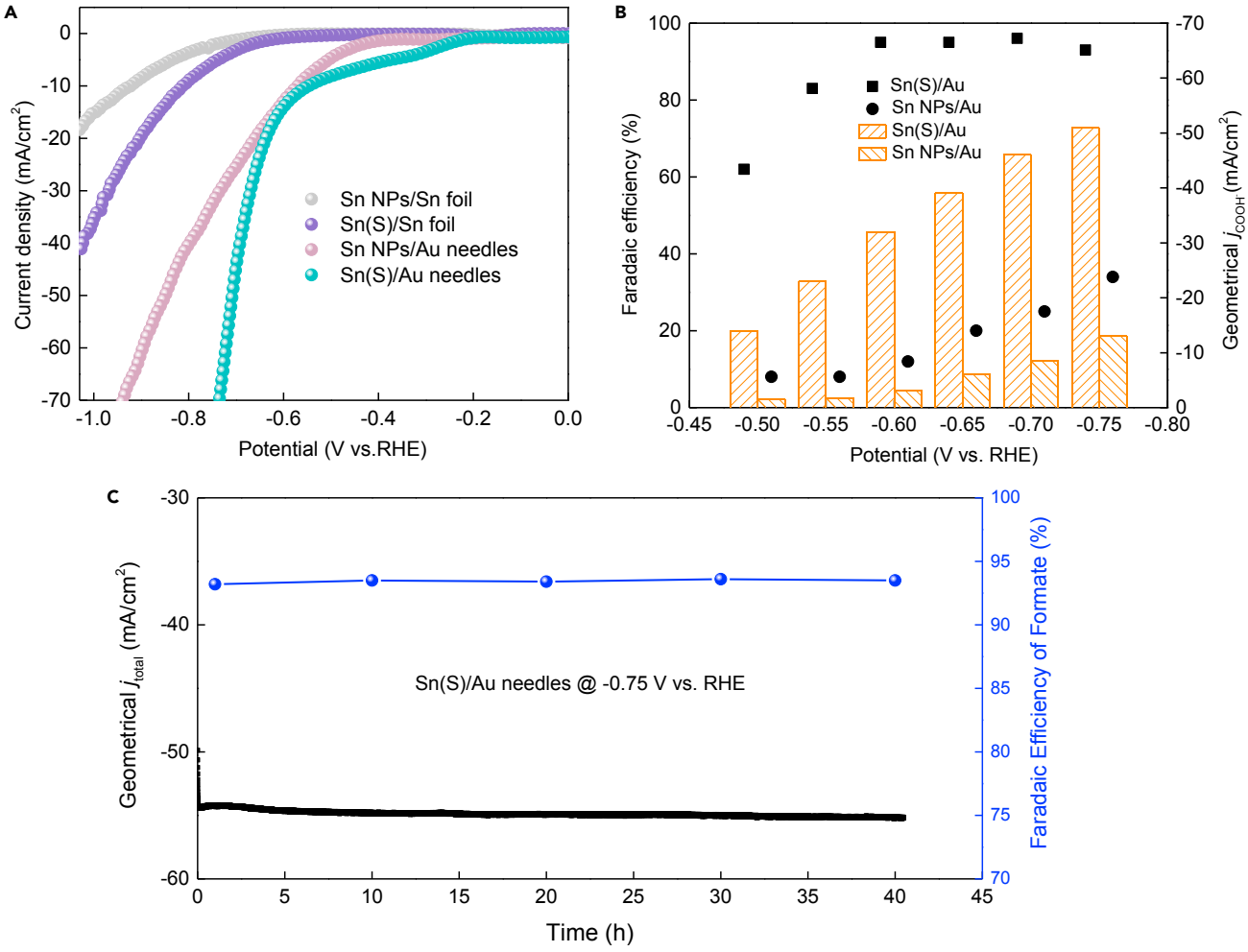

Figure 5. Performance of Sulfur-Modulated Tin Catalysts and Controls in a Three-Electrode Configuration in CO_2 Saturated 0.1 M $KHCO_3$ Aqueous Electrolyte

(A) The CO_2RR polarization curve of catalysts loaded on Au needles and Sn foil, respectively.

(B) Potential dependence (with iR corrected) of Faradaic efficiencies and current densities for CO_2RR on Sn(S)/Au (squares) and Sn NPs/Au (circles).

(C) Stability test of Sn(S) at −0.75 V versus RHE (iR corrected).

with a total current density of 55 mA cm^{-2} (normalized to geometric surface area) is obtained at −0.75 V versus RHE for Sn(S)/Au. This formate partial current density on Sn(S)/Au represents higher than that of the best non-noble metal (Tables 1 and S8). To evaluate the effect of surface area, we measured the ECSA for Sn(S)/Au, Sn NPs/Au, and sputtered Sn/Au from the electrochemical double-layer capacitance of the catalytic surface (Figure S8). From ECSA normalized performance of CO_2 reduction to formate, the high catalytic activity of Sn(S)/Au includes an appreciable intrinsic (not surface-area-related) contribution. The partial current density for formate on Sn(S)/Au, normalized by ECSA, is between 1.2 and 3 times higher than that of Sn NPs/Au and sputtered Sn/Au (Figure S9 and Table S9). To experimentally probe the reaction intermediates, we observed formate in the interfacial region (1,300–1,400 cm^{-1}) by *in situ* attenuated total reflection mode Fourier transform infrared (ATR-FTIR) (Figure S18).[39,40] We note that a bound intermediate formate species (HCOO*) has been reported before in the literature,[39] but unfortunately we were not able to detect this species. While our *in situ* ATR-FTIR was inconclusive for bound HCOO* intermediates, there were no peaks that could be attributed to

the bound or interfacial carboxylate intermediate (COOH*). These results qualitatively agree well with our simulations, whereby the reaction pathways are based on prior literature.[13,25]

One of the most critical aspects of formate production from CO_2RR is the deactivation of the catalyst over time. Although Pd catalysts only require low potential for CO_2 to formate (Table 1), CO poisoning has limited its potential practical application.[13] To characterize the performance stability of the Sn(S) catalysts, we performed CO_2 reduction with the Sn(S) catalyst under a constant potential of −0.75 V versus RHE continuously for 40 hours. We observed no appreciable decrease (<2%) in current (Figure 5C) during this time interval. Furthermore, we performed potential-cycling experiments that showed no degradation in activity over five 1-hr cycles (Figure S20). We also confirmed the Faradaic efficiency for formate generation was nearly quantitative (>93%) throughout the electrocatalytic process. This formate partial current density on Sn(S)/Au is higher than the previously reported non-noble metal catalysts in aqueous solution (Table 1),[2,30] confirming that the undercoordinated tin sites greatly increased the catalytic activity of CO_2 to formate.

EXPERIMENTAL PROCEDURES

DFT Calculations

Initially, we started by simulating a SnS slab.[41] It is characterized by an orthorhombic herzenbergite structure where the Sn^{2+} ion adopts a tetrahedral geometry coordinating three S^{2-} ions with the Sn $5s^2$ lone pair occupying the fourth position.[42] We then gradually increased the Sn content in the SnS crystal structure by randomly replacing S atoms with Sn atoms such that the resultant structures had 37.5%, 25%, and 12.5% sulfur content. The atomic positions and unit cell parameters of all structures were relaxed and fully optimized using DFT (Figure S17). The optimized structural parameters for SnS (Tables S1 and S2) served as a benchmark for the validity of further calculations. The {100} facet was used for all slabs with a 4 × 4 × 4 atom slab and 20 Å between mirror images in the z axis in the unit cell. To justify the facet choice, we calculated the surface energies for the {100}, {110}, {111}, {211}, and {311} facets of SnS (Table S7). It was found that the {100} facet has the lowest surface energy and is thus expected to be the most stable surface. Bader charge analysis shows electron density of the bound oxygen atoms is slightly higher on slightly doped Sn(S), suggesting a stronger Sn–O intermediate bond (Table S5).

X-Ray Absorption Measurements

The Sn K-edge spectra were collected at the 06ID-1 Hard X-ray MicroAnalysis (HXMA) beamline and soft X-ray Microcharacterization (SXMRB) beamline from Canadian Light Source. *In situ* Sn-L_3 edge and S K-edge XANES spectra were collected at the soft X-ray Microcharacterization (SXMRB) beamline from Canadian Light Source. *Ex situ* Sn L_3-edge spectra were collected at Beamline 10.3.2 from the Advanced Light Source.

Preparation of Sn(S) on Au Needles

Gold electrodes were prepared through an electrodeposition process using a solution containing $HAuCl_4$ (99.99%, Sigma) and HCl (TraceSELECT) solution.[3] SnS_x was deposited at 90°C using tetrakis(dimethylamino)-tin(IV) (TDMASn, 99.99% Sn; Strem Chemicals) and H_2S at a constant growth rate of 0.035 nm per cycle measured by ellipsometry. TDMASn was held at 65°C. Nitrogen was used as a carrier gas (99.9999% pure, Carbagas) with a flow rate of 10 sccm.[43–45] Cyclic voltammetry measurements from 0.4 V to −1.0 V versus RHE at 50 mV/s were performed in CO_2 saturated 0.1 M $KHCO_3$ electrolyte for three cycles to activate and partially remove sulfur atoms from

the as-prepared SnS_x/Au electrode. The CO_2 reduction performance was then carried out in the same electrolyte.

Preparation of Sn Nanoparticles on Au Needles

Electrophoretic deposition was implemented to uniformly deposit Sn NPs on nanostructured Au electrode.[34,46,47] Specially, 10 mg/L Sn NPs in ethanol were placed in the ultrasonic bath for 50 min and centrifuged for 30 min at 4,000 rpm to remove large NPs from the suspension. Finally, a DC power supply of 20 V was applied for 20 min to deposit Sn NPs (Figure S7).

Electrocatalytic Reduction of CO_2

All CO_2 reduction experiments were performed using a three-electrode system connected to an electrochemical workstation (Autolab PGSTAT302N). Ag/AgCl (with saturated KCl as the filling solution) and platinum mesh were used as reference and counter electrodes, respectively. Electrode potentials were converted to the RHE reference scale using $E_{RHE} = E_{Ag/AgCl} + 0.197\ V + 0.0591 \times pH$. The potentials were iR corrected using electrochemical impedance spectroscopy (Figure S16).

The electrolyte was 0.1 M $KHCO_3$ saturated with CO_2. Formate was quantified on gas chromatography with mass spectrometry (PerkinElmer Clarus 600 GC-MS System). Assuming that two electrons are needed to produce one formate molecule, the Faradaic efficiency was calculated as follows: Faradaic efficiency = $2F \times n_{formate}/Q = 2F \times n_{formate}/(I \times t)$, where F is the Faraday constant, I is the current, t is the running time, and $n_{formate}$ is the total amount of formate produced (in moles).

Characterization

High-resolution TEM (HRTEM) images were taken on an FEI monochromated F20 UT Tecnai microscope operated at 200 kV. STEM elemental mapping of samples were taken on a FEI Titan 80–300 environmental (scanning) electron microscope (E(S) TEM), with a spot size of 6 and a C2 aperture size of 70 μm. Scanning electron microscopy (SEM) was performed on a Hitachi SU8230 scanning electron microscope operated at 1.0 kV. Powder X-ray diffraction patterns were obtained with a MiniFlex600 instrument. XPS measurements were carried out on a Thermo Scientific K-Alpha system, with a 300 μm spot size, 75 eV pass energy, and energy steps of 0.05 eV, and aluminum anode X-ray excitation. The Shirley algorithm was used to fit the background. Then the atomic ratio was computed by summing over the curves over the background and taking into account the absorption cross-section of Sn and S to determine relative ratios from their intensities (Figure S10). The *in situ* spectroelectrochemical (ATR-FTIR) measurements were performed on a Bruker IFS 66/S spectrometer. For the *in situ* technique, a sealed electrochemical cell (Figure S18) with Pt as counter electrode, Sn(S) as working electrode, and Ag/AgCl reference electrode was mounted in the spectrometer. The system was continuously flushed with CO_2 saturated 0.1 M $KHCO_3$. Sn(S) was deposited onto a germanium crystal (1 × 1 × 0.2 cm parallelepiped, angle 45°C) as reflection element. During the spectroscopic recording, a constant potential was applied (−0.3 V, −0.5 V, and −0.7 V versus RHE, respectively) (Figure S18).

SUPPLEMENTAL INFORMATION

Supplemental Information includes Supplemental Experimental Procedures, 20 figures, and 9 tables and can be found with this article online at https://doi.org/10.1016/j.joule.2017.09.014.

AUTHOR CONTRIBUTIONS

E.H.S. and P.Y. supervised the project. X.Z. designed the experiments. P.D.L. carried out the simulation parts. X.Z., P.D.L., N.B., and M.N.B. performed the X-ray measurements. M.B.R. carried out *in situ* Raman measurements. Yifan Li and Yuzhang Li performed the TEM measurements. O.V. carried out the XPS measurements. X.Z., F.P.G.d.A., B.Z., M.L., T.Z., and C.T.D. performed electrochemical measurements. P.S. carried out *in situ* FTIR measurements. Y.C. and X.D. revised the manuscript. All authors discussed the results and assisted during manuscript preparation.

ACKNOWLEDGMENTS

This work was supported by the Ontario Research Fund - Research Excellence Program (RE08-034); NSERC (RGPIN-2017-06477); and the CIFAR Bio-Inspired Solar Energy program (FL-000560). This work was also supported by the Director, Office of Science, Office of Basic Energy Sciences, Chemical Sciences, Geosciences, & Biosciences Division, of the U.S. Department of Energy under contract no. DE-AC02-05CH11231, FWP no. CH030201 (Catalysis Research Program), National Basic Research Program of China (2014CB931703), and the Natural Science Foundation of China (51471115, 51571149). X.Z. acknowledges a scholarship from the China Scholarship Council (CSC) (20140625004). P.D.L. acknowledges NSERC for financial support in the form of the Canada Graduate Scholarship – Doctoral (CGS-D). The CLS is supported by the Natural Sciences and Engineering Research Council of Canada, the National Research Council Canada, the Canadian Institutes of Health Research, the Province of Saskatchewan, Western Economic Diversification Canada, and the University of Saskatchewan. The authors thank Y.J. Pang, J. Li, and Z.Q. Zhang for fruitful discussions, R. Wolowiec and D. Kopilovic for their help during the course of study. DFT computations were performed using the IBM BlueGene/Q supercomputer at the SciNet HPC Consortium provided through the Southern Ontario Smart Computing Innovation Platform (SOSCIP). We acknowledge M. Marcus and the use of Beamline 10.3.2 at the Advanced Light Source for collection of XAS data. The Advanced Light Source and Molecular Foundry are supported by the Director, Office of Science, Office of Basic Energy Sciences, of the U.S. Department of Energy under contract no. DE-AC02-05CH11231.

Received: June 17, 2017
Revised: August 19, 2017
Accepted: September 25, 2017
Published: October 16, 2017

REFERENCES

1. Lin, S., Diercks, C.S., Zhang, B., Kornienko, N., Yang, P., and Yaghi, O.M. (2015). Covalent organic frameworks comprising cobalt porphyrins for catalytic CO_2 reduction in water. Science *349*, 1208–1215.

2. Mccollum, D.L., Jewell, J., Krey, V., Ramanathan, V., Fay, M., and Riahi, K. (2016). Quantifying uncertainties influencing the long-term impacts of oil prices on energy markets and carbon emissions. Nat. Energy *1*, 1–7.

3. Liu, M., Pang, Y., Zhang, B., De Luna, P., Voznyy, O., Xu, J., Zheng, X., and Sargent, E. (2016). Enhanced electrocatalytic CO_2 reduction via field-induced reagent concentration. Nature *537*, 382–386.

4. Gao, S., Lin, Y., Jiao, X., Sun, Y., Luo, Q., and Zhang, W. (2016). Partially oxidized atomic cobalt layers for carbon dioxide electroreduction to liquid fuel. Nature *529*, 68–71.

5. Benson, E.E., Kubiak, C.P., Sathrum, A.J., and Smieja, J.M. (2009). Electrocatalytic and homogeneous approaches to conversion of CO_2 to liquid fuels. Chem. Soc. Rev. *38*, 89–99.

6. Li, C.W., Ciston, J., and Kanan, M.W. (2014). Electroreduction of carbon monoxide to liquid fuel on oxide derived nanocrystalline copper. Nature *508*, 504–507.

7. Goeppert, A., Czaun, M., Jones, J.P., Surya Prakash, G.K., and Olah, G.A. (2014). Recycling of carbon dioxide to methanol and derived products - closing the loop. Chem. Soc. Rev. *2*, 189–194.

8. Reda, T., Plugge, C.M., Abram, N.J., and Hirst, J. (2008). Reversible interconversion of carbon dioxide and formate by an electroactive enzyme. Proc. Natl. Acad. Sci. USA *105*, 10654–10658.

9. Wang, W., Himeda, Y., Muckerman, J., and Fujita, E. (2015). CO_2 hydrogenation to formate and methanol as an alternative to photo- and electrochemical CO_2 reduction. Chem. Rev. *115*, 12936–12973.

10. Verma, S., Kim, B., Jhong, H.R., Ma, S., and Kenis, P.J. (2016). A gross-margin model for defining technoeconomic benchmarks in the

electroreduction of CO_2. ChemSusChem *9*, 1972–1979.

11. Lu, X., Leung, D.Y.C., Wang, H., Leung, M.K.H., and Xuan, J. (2014). Electrochemical reduction of carbon dioxide to formic acid. ChemElectroChem *1*, 836–849.

12. Chen, Y., and Kanan, M.W. (2012). Tin oxide dependence of the CO_2 reduction efficiency on tin electrodes and enhanced activity for tin/tin oxide thin-film catalysts. J. Am.Chem. Soc. *134*, 1986–1989.

13. Klinkova, A., De Luna, P., Dinh, C.T., Voznyy, O., Larin, E., and Kumacheva, E. (2016). Rational design of efficient palladium catalysts for electroreduction of carbon dioxide to formate. ACS Catal. *6*, 8115–8120.

14. Kim, D., Resasco, J., Yu, Y., Asiri, A.M., and Yang, P. (2014). Synergistic geometric and electronic effects for electrochemical reduction of carbon dioxide using gold-copper bimetallic nanoparticles. Nat. Commun. *5*, 4948.

15. Zhang, S., Kang, P., and Meyer, T.J. (2014). Nanostructured tin catalysts for selective electrochemical reduction of carbon dioxide to formate. J. Am. Chem. Soc. *136*, 1734–1737.

16. Lee, S., Kim, D., and Lee, J. (2015). Electrocatalytic production of C3-C4 compounds by conversion of CO_2 on a chloride-induced bi-phasic Cu_2O-Cu catalysts. Angew. Chem. Int. Ed. *127*, 14914–14918.

17. Zhu, Q., Ma, J., Kang, X., Sun, X., Liu, H., and Hu, J. (2016). Efficient reduction of CO_2 into formic acid on a lead or tin electrode using an ionic liquid catholyte mixture. Angew. Chem. Int. Ed. *55*, 9012–9016.

18. Won da, H., Choi, C.H., Chung, J., Chung, M.W., Kim, E.H., and Woo, S.I. (2015). Rational design of a hierarchical tin dendrite electrode for efficient electrochemical reduction of CO_2. ChemSusChem *8*, 3092–3098.

19. Min, X., and Kanan, M.W. (2015). Pd-catalyzed electrohydrogenation of carbon dioxide to formate: high mass activity at low overpotential and identification of the deactivation pathway. J. Am. Chem. Soc. *137*, 4701–4708.

20. Kortlever, R., Peters, I., Koper, S., and Koper, M.T. (2015). Electrochemical CO_2 reduction to formic acid at low overpotential and with high faradaic efficiency on carbon-supported bimetallic Pd–Pt nanoparticles. ACS Catal. *5*, 3916–3923.

21. Li, F., Chen, L.P., Knowles, G.R., MacFarlane, D., and Zhang, J. (2016). Hierarchical mesoporous SnO_2 nanosheets on carbon cloth: a robust and flexible electrocatalyst for CO_2 reduction. Angew. Chem. Int. Ed. *128*, 1–6.

22. Pander, J.E., Baruch, M.F., and Bocarsly, A.B. (2016). Probing the mechanism of aqueous CO_2 reduction on post-transition-metal electrodes using ATR-IR spectroelectrochemistry. ACS Catal. *6*, 7824–7833.

23. Hollingsworth, N., Taylor, S.F., Galante, M.T., Jacquemin, J., Longo, C., Holt, K.B., de Leeuw, N.H., and Hardacre, C. (2015). Reduction of carbon dioxide to formate at low overpotential using a superbase ionic liquid. Angew. Chem. Int. Ed. *54*, 14164–14168.

24. Lee, C.H., and Kanan, M.W. (2015). Controlling H^+ vs CO_2 reduction selectivity on Pb electrodes. ACS Catal. *5*, 465–469.

25. Yoo, J.S., Christensen, R., Vegge, T., Norskov, J.K., and Studt, F. (2016). Theoretical insight into the trends that guide the electrochemical reduction of carbon dioxide to formic acid. ChemSusChem *9*, 358–363.

26. Hirunsit, P. (2013). Electroreduction of carbon dioxide to methane on copper, copper silver, and copper–gold catalysts: a DFT study. J. Phys. Chem. C *117*, 8262–8268.

27. Rosen, J., Hutchings, G.S., Lu, Q., Rivera, S., Zhou, Y., Vlachos, D.G., and Jiao, F. (2015). Mechanistic insights into the electrochemical reduction of CO_2 to CO on nanostructured Ag surfaces. Azcs Catal. *5*, 4293–4299.

28. Mistry, H., Varela, A.S., Bonifacio, C.S., Strasser, P., and Cuenya, B. (2016). Highly selective plasma activated copper catalysts for carbon dioxide reduction to ethylene. Nat. Commun. *7*, 12123–12130.

29. Kortlever, R., Shen, J., Schouten, K.J., Calle-Vallejo, F., and Koper, M.T. (2015). Catalysts and reaction pathways for the electrochemical reduction of carbon dioxide. J. Phys. Chem. Lett. *6*, 4073–4082.

30. Li, Y., Wang, H., Xie, L., Liang, Y., Hong, G., and Dai, H. (2011). MoS_2 nanoparticles grown on graphene: an advanced catalyst for the hydrogen evolution reaction. J. Am. Chem. Soc. *133*, 7296–9299.

31. Li, F., Chen, L., Xue, M., William, T., Zhang, Y.R., and MacFarlane, D. (2017). Towards a better Sn: efficient electrocatalytic reduction of CO_2 to formate by Sn/SnS_2 derived from SnS_2 nanosheets. Nano Energy *31*, 270–277.

32. Lei, F., Liu, W., Sun, Y., Xu, J., Liu, K., and Liang, L. (2016). Metallic tin quantum sheets confined in graphene toward high-efficiency carbon dioxide electroreduction. Nat. Commun. *7*, 12697.

33. Chen, L.D., Urushihara, M., Chan, K., and Nørskov, J.K. (2016). Electric field effects in electrochemical CO_2 reduction. ACS Catal. *6*, 7133–7139.

34. Vinson, J., and Rehr, J.J. (2012). Ab initio Bethe-Salpeter calculations of the X-ray absorption spectra of transition metals at the L-shell edges. Phys. Rev. B *2*, 78–84.

35. Moreno, M.S., Egerton, R.F., Rehr, J.J., and Midgley, P.A. (2005). Electronic structure of tin oxides by electron energy loss spectroscopy and real-space multiple scattering calculations. Phys. Rev. B *71*, 035103.

36. Liu, Z., Handa, K., Kaibuchi, K., Tanaka, Y., and Kawai, J. (2004). Comparison of the Sn L edge X-ray absorption spectra and the corresponding electronic structure in Sn, SnO, and SnO2. J. Electron Spectros. Relat. Phenomena *135*, 155–158.

37. Vinson, J., Kas, J.J., Vila, F.D., Rehr, J.J., and Shirley, E.L. (2012). Theoretical optical and x-ray spectra of liquid and solid H_2O. Phys. Rev. B *85*, 045101.

38. Kapilashrami, M., Kronawitter, C.X., Torndahl, T., Lindahl, J., Hultqvist, A., and Wang, W.C. (2012). Soft X-ray characterization of $Zn_{(1-x)}Sn_{(x)}O_{(y)}$ electronic structure for thin film photovoltaics. Phys. Chem. Chem. Phys. *14*, 10154–10159.

39. Baruch, M.F., Pander, J.E., III, White, J.L., and Bocarsly, A.B. (2015). Mechanistic insights into the reduction of CO_2 on tin electrodes using in situ ATR-IR spectroscopy. ACS Catal. *5*, 3148–3156.

40. Figueiredo, M.C., Ledezma-Yanez, I., and Koper, M.T. (2016). In situ spectroscopic study of CO_2 electroreduction at copper electrodes in acetonitrile. ACS Catal. *6*, 2382–2392.

41. Burton, L.A., and Walsh, A. (2012). Phase stability of the Earth-abundant tin sulfides SnS, SnS2, and Sn2S3. J. Phys. Chem. C *116*, 24262–24267.

42. Klimm, K.C., Kohn, S.A., O'Dell, L.E., Botcharnikov, R.E., and Smith, M. (2012). The dissolution mechanism of sulphur in hydrous silicate melts. I: assessment of analytical techniques in determining the sulphur speciation in iron-free to iron-poor glasses. Chem. Geol. *322*, 237–249.

43. Wang, D., Yang, J., Liu, J., Li, X., Li, R., and Cai, M. (2014). Atomic layer deposited coatings to significantly stabilize anodes for Li ion batteries: effects of coating thickness and the size of anode particles. J. Mater. Chem. A *2*, 2306.

44. Sun, Y., Sun, Z., Gao, S., Cheng, H., Liu, Q., and Lei, F. (2014). All-surface-atomic-metal chalcogenide sheets for high-efficiency visible-light photoelectrochemical water splitting. Adv. Energy Mater. *4*, 1300611–1300622.

45. Dasgupta, N.P., Meng, X., Elam, J.W., and Martinson, A.B. (2015). Atomic layer deposition of metal sulfide materials. Acc. Chem. Res. *48*, 341–348.

46. Wang, G.J., and Chou, S.W. (2010). Electrophoretic deposition of uniformly distributed TiO_2 nanoparticles using an anodic aluminum oxide template for efficient photolysis. Nanotechnology *21*, 115206.

47. Besra, L., and Liu, M. (2007). A review on fundamentals and applications of electrophoretic deposition (EPD). Progr. Mater. Sci. *52*, 1–61.

JOUL, Volume *1*

Supplemental Information

Sulfur-Modulated Tin Sites Enable Highly Selective Electrochemical Reduction of CO_2 to Formate

Xueli Zheng, Phil De Luna, F. Pelayo García de Arquer, Bo Zhang, Nigel Becknell, Michael B. Ross, Yifan Li, Mohammad Norouzi Banis, Yuzhang Li, Min Liu, Oleksandr Voznyy, Cao Thang Dinh, Taotao Zhuang, Philipp Stadler, Yi Cui, Xiwen Du, Peidong Yang, and Edward H. Sargent

Supplementary Figures and Tables

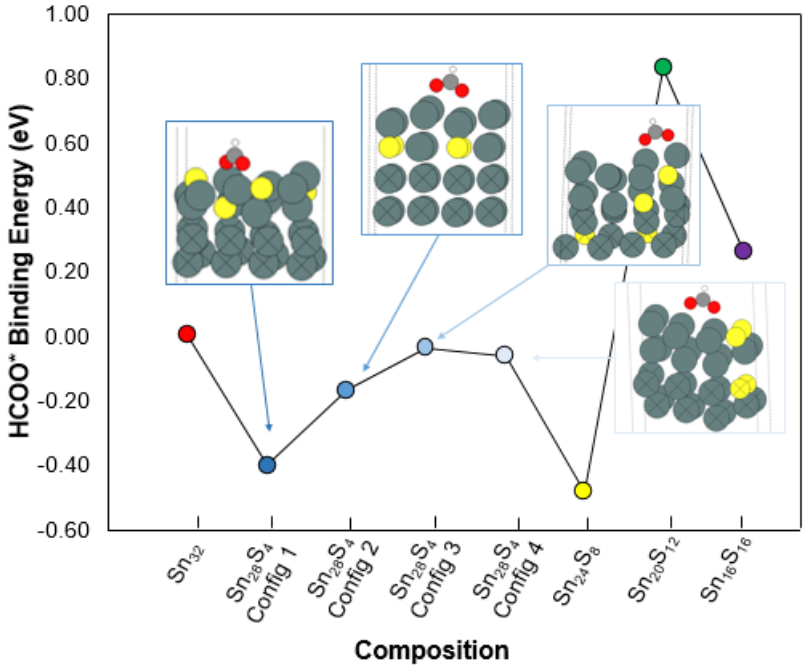

Figure S1. Plot of intermediate (HCOO*) binding energy with respect to different configurations of Sn_xS_y.

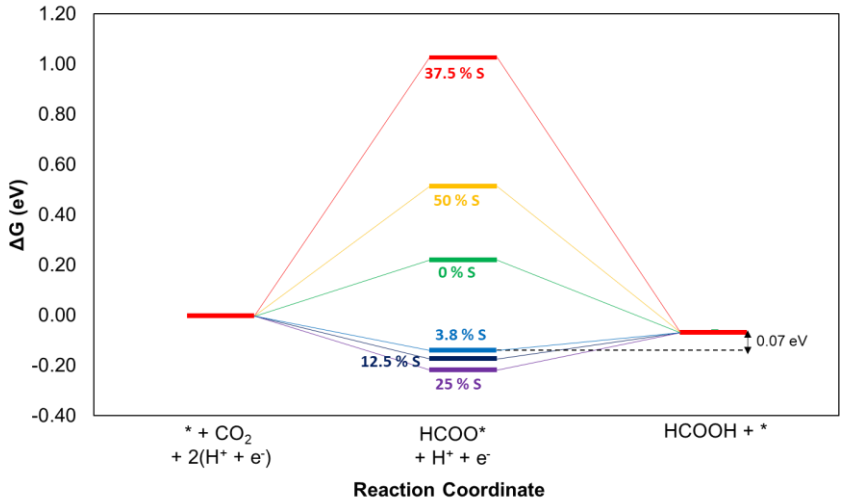

Figure S2. The reaction energy diagram for electroreduction of CO_2 to formic acid with Sn(S) catalysts of various sulfur content.

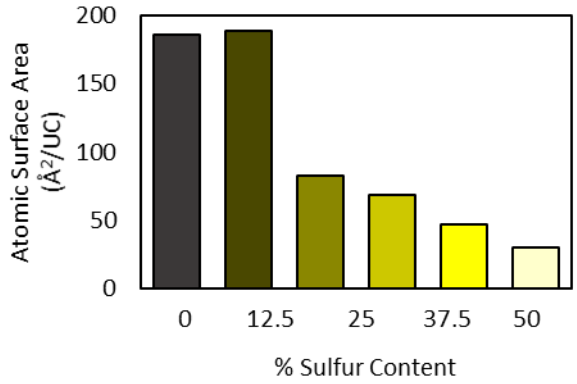

Figure S3. Atomic surface area for the different slab models normalized to the number of Sn atoms.

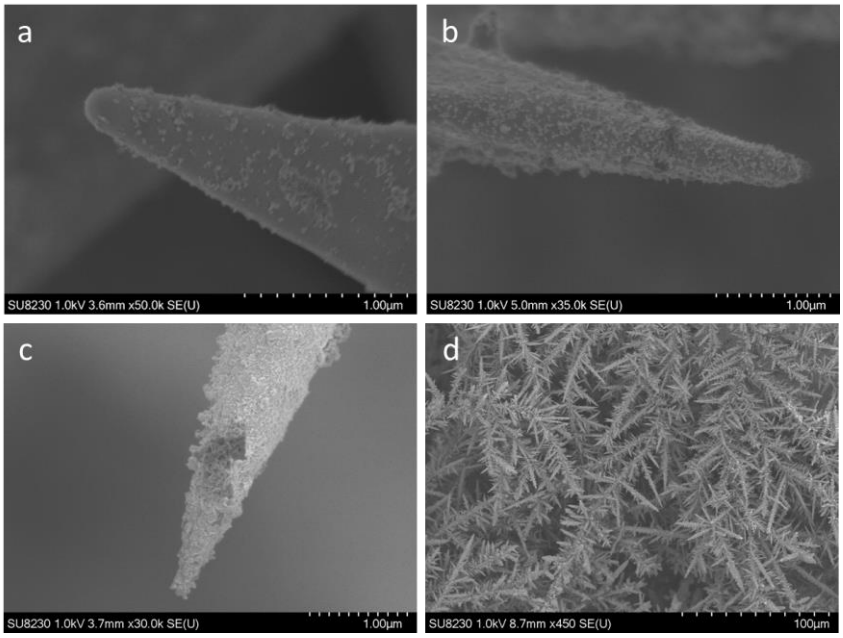

Figure S4. SEM images of SnS_x deposited via (a) 50 cycles, (b) 200 cycles and (c) (d) 500 cycles of ALD on Au needles. It was found that 500 cycles were enough to fully cover Au needles.

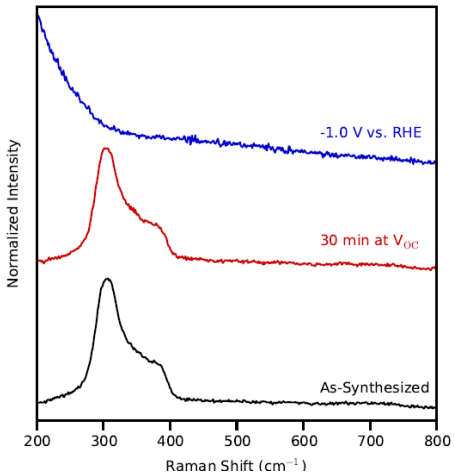

Figure S5. *In situ* Raman spectra of Sn(S) deposited via 500 cycles of ALD on Au needles at open circuit (red line), and -1.0 V vs. RHE (blue line). Raman spectra at -1.0 V vs. RHE confirmed that the bulk and vast majority of SnS_x is reduced to Sn metal at high potentials. Note that because Raman is not explicitly a surface technique, it is unlikely to observe trace Sn-S bonding vibrations, especially in comparison to the bulk crystalline vibrations that are easily observed in the bulk ALD SnS_x. In other words, it cannot be used to rule out the presence of S atoms near the surface.

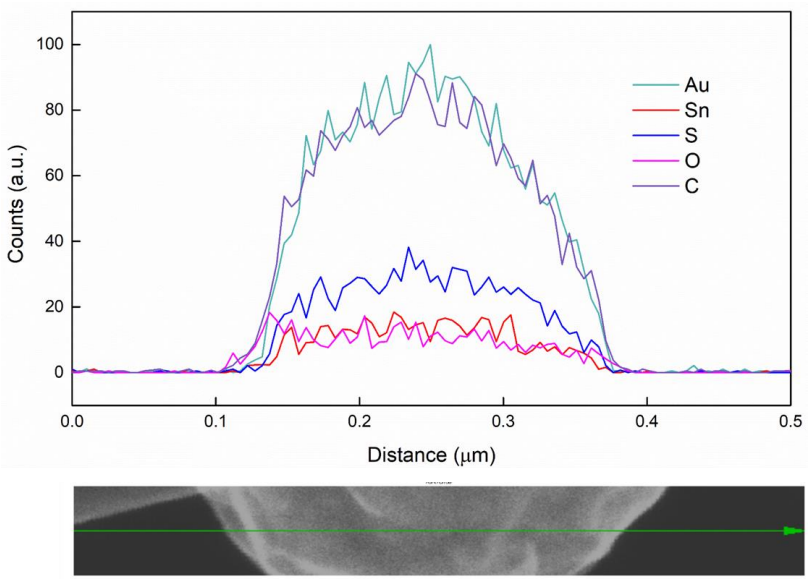

Figure S6. Energy dispersive spectroscopy line-scan of Sn(S) after reaction.

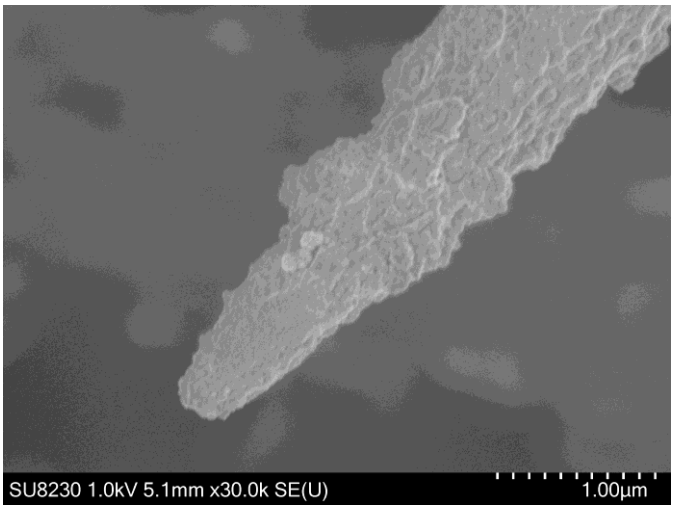

Figure S7. SEM image of uniformly deposited Sn nanoparticles on Au needles by electrophoretic deposition.

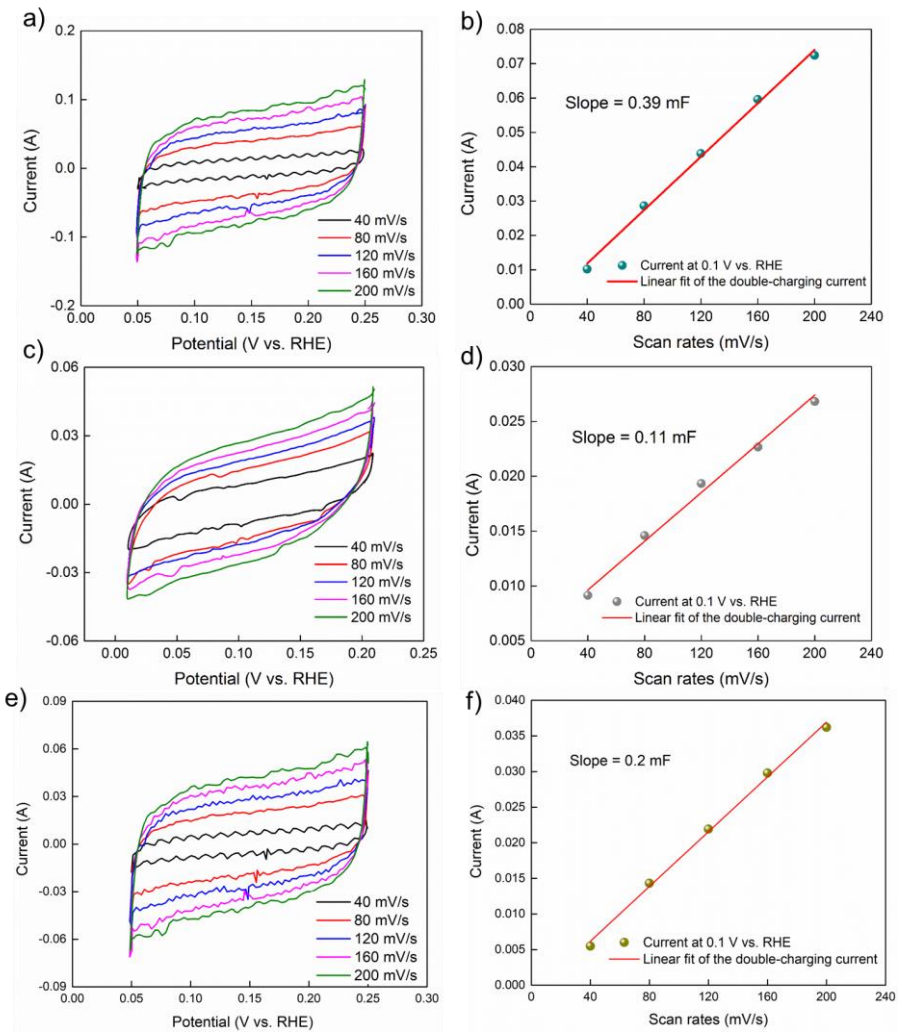

Figure S8. Electrochemical surface area measurement. a, b, Determination of double-layer capacitance over a range of scan rates for Sn(S)/Au electrode. c, d, Determination of double-layer capacitance over a range of scan rates for Sn NPs/Au electrode. e, f, Determination of double-layer capacitance over a range of scan rates for Sputtering Sn/Au electrode. a, c, e, Cyclic voltammagrams taken over a range of scan rates. b, d, f, Current due to double-layer charging plotted against cyclic voltammetry scan rate.

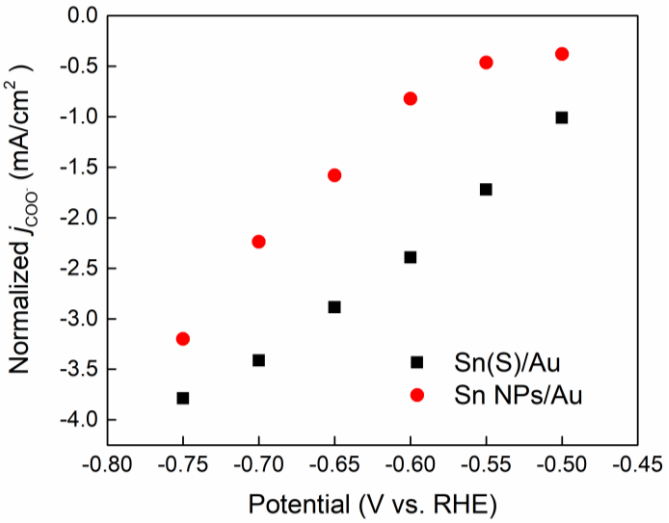

Figure S9. Surface-area-normalized current densities for formate production for Sn(S)/Au (black) and Sn NPs/Au (red), respectively.

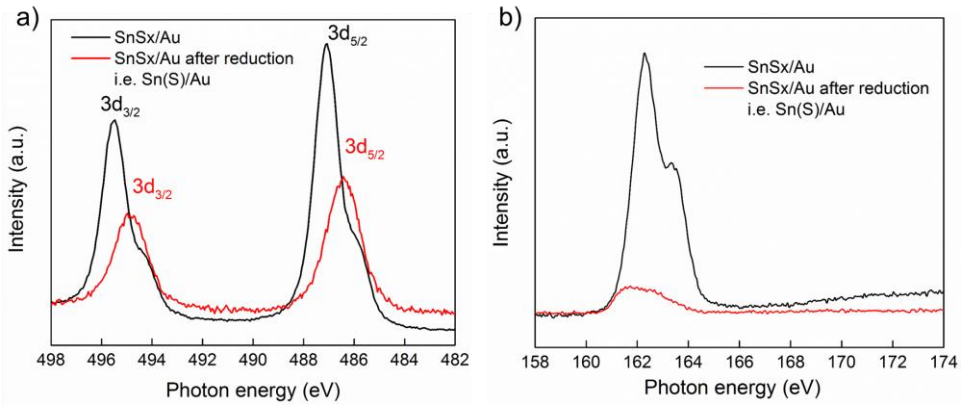

Figure S10. (a) Sn 3d and (b) S 2p XPS spectra of SnS_x/Au before and after reduction. The Sn 3d and S 2p spectra of SnS_x/Au before and after reduction revealed the partial removal of sulfur throughout the reduction process. Based on the results from XPS analysis, the content of S in the Sn(S) catalyst was calculated to be 3.2 at%.

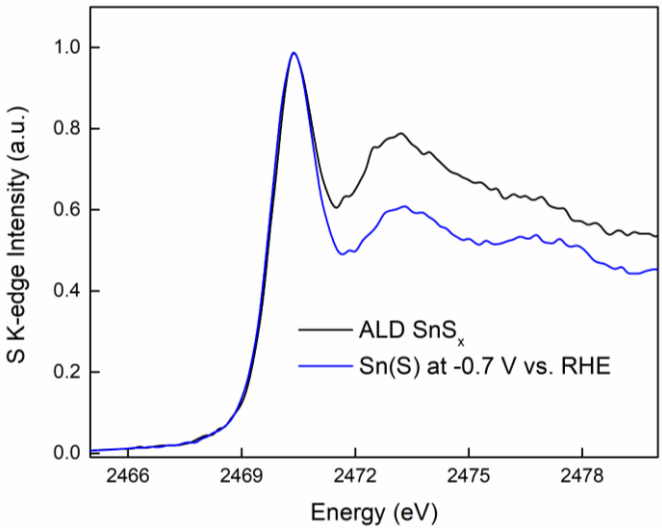

Figure S11. *In situ* S K-edge of ALD SnS_x (black line) and Sn(S) at -0.7 V vs. RHE (blue line).

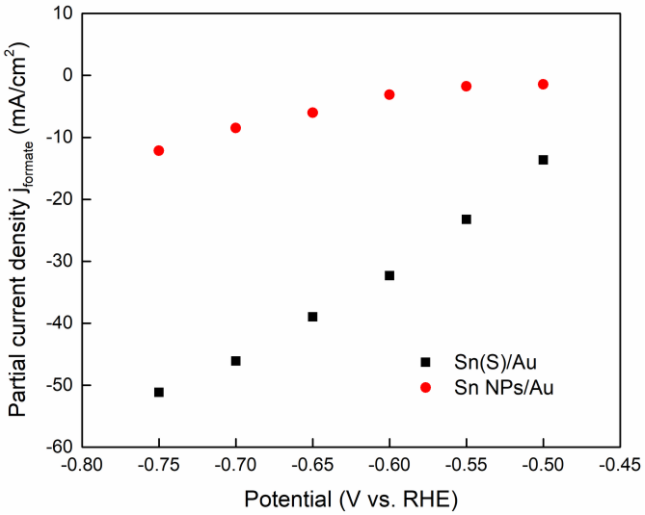

Figure S12. Partial current densities for formate production for Sn(S)/Au (black) and Sn NPs/Au (red), respectively.

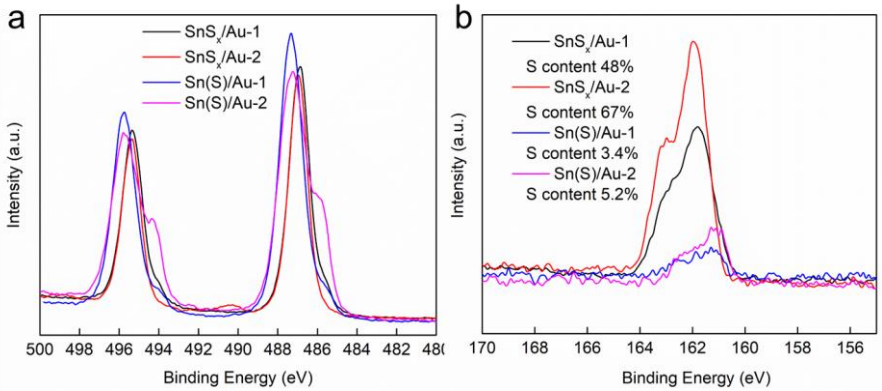

Figure S13. (a) Sn 3d and (b) S 2p XPS spectra of SnS_x/Au and Sn(S)/Au after reduction. Different compositions of the SnS_x were synthesized by changing the ratio of tetrakis(dimethylamino)-tin(IV) (TDMASn) and H_2S during atomic layer deposition (TDMASn:H_2S=1:1 i.e. SnS_x/Au-1 and TDMASn:H_2S=1:2 i.e. SnS_x/Au-2). X-ray photoelectron spectroscopy (XPS) was used to determine the ratio of Sn and S before the initial reduction step (The content of surfur for SnS_x/Au-1 and SnS_x/Au-2 is 48% and 67%, respectively). The Sn 3d and S 2p spectra of SnS_x/Au before and after reduction for one hour revealed the partial removal of sulfur throughout the reduction process (Figure S13). The Shirley algorithm was used to fit the background. Specifically, the atomic ratio is computed by summing over the curves over the background and taking into account the absorption cross-section of Sn and S to determine relative ratios from their intensities. Based on the calculation from XPS analysis, the content of S in the Sn(S)/Au-1 and Sn(S)/Au-2 after reaction was calculated to be 3.4 at% and 5.2 at%, respectively. We also performed the CO_2 reduction reaction of of Sn(S)/Au-1 and Sn(S)/Au-2 in 0.1 M $KHCO_3$ electrolyte. The Faradaic efficiency of Sn(S)/Au-1 and Sn(S)/Au-2 approached ~95% when applying potential at -0.75 V vs. RHE (iR-corrected). These results show that the specific doping amount between 3.4% and 5.2% have a negligible impact on Faradaic efficiency. These results agree well with the computational simulations that showed low sulfur doping amounts are thermodynamically favourable for formate production.

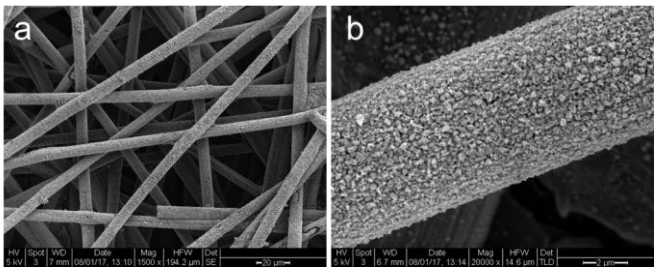

Figure S14. SEM images of Sn(S) activated on carbon paper after reaction.

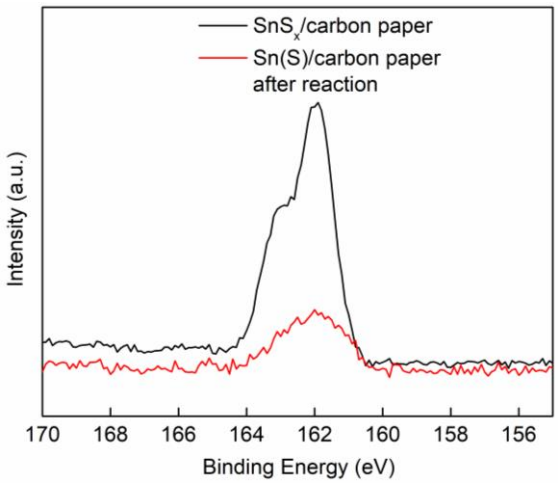

Figure S15. S 2p XPS of SnS_x/carbon paper and Sn(S) on carbon paper after reaction. To avoid the effect of Au substrates and thus the potential increased sulfur content adhering to gold, we deposited SnS_x on carbon paper via atomic layer deposition as a control sample. SEM images showed that SnS_x thin films and Sn(S) after reaction were deposited uniformly on carbon paper (Figure S14). We then performed cyclic voltammetry (CV) measurements from 0.4 V to -1.0 V vs. RHE at 50 mV/s in CO_2 saturated 0.1 M $KHCO_3$ electrolyte for 3 cycles to activate and partially remove sulfur atoms from the as-prepared SnS_x/carbon paper electrode. The content of S in the Sn(S)/carbon paper after reaction for 1 hour was calculated to be 4.6 at% (Figure S15). The amount of S in the Sn(S)/carbon paper system is similar to the Sn(S)/Au system and not significantly decreased which suggests that the sulfur is present at the surface of the Sn(S).

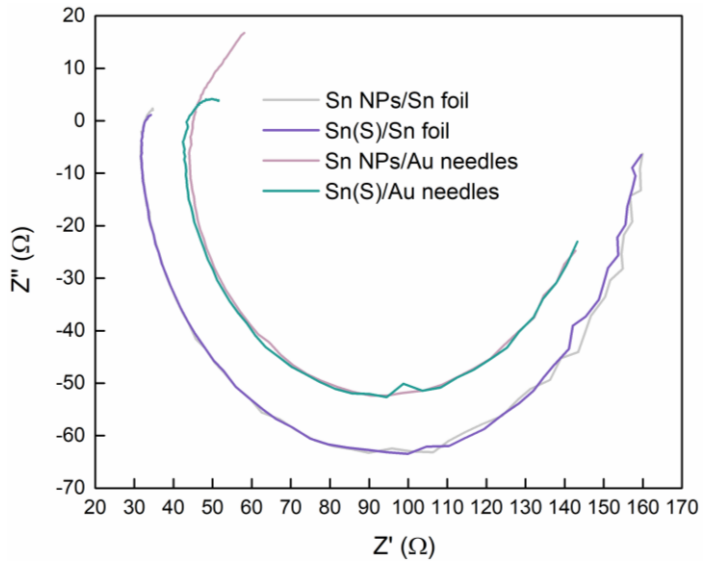

Figure S16. Electrochemical impedance spectroscopy (EIS) data for catalysts loaded on Au needles and Sn foil, respectively in three-electrode configuration in CO_2 saturated 0.1 M $KHCO_3$ aqueous electrolyte.

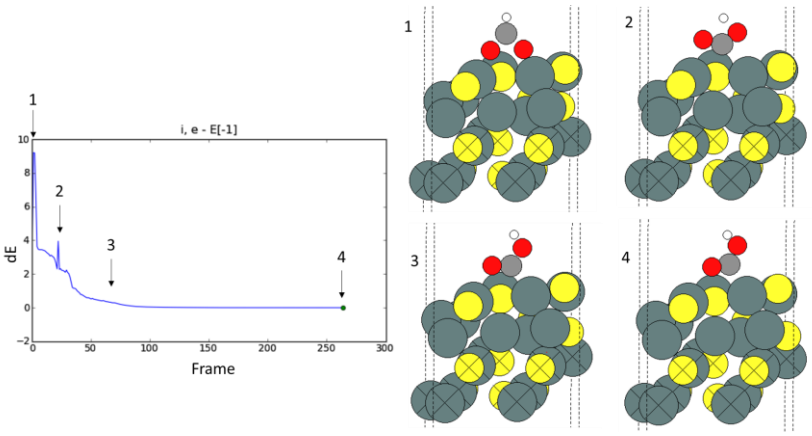

Figure S17. Plot of change in energy with respect to optimization step, i.e Frame for $Sn_{20}S_{12}$-HCOO* system (left). Snapshots from the geometry relaxation at the initial (1), 25 steps (2), 60 steps (3), and final configuration (4).

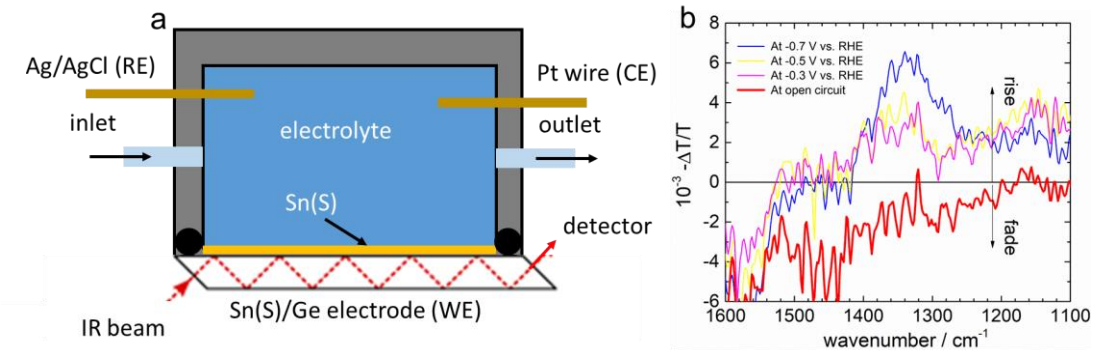

Figure S18. (a) Schematic illustration of the *in situ* liquid cell experimental setup for FTIR. (b) *In-situ* FTIR spectra plot during applying different potentials.

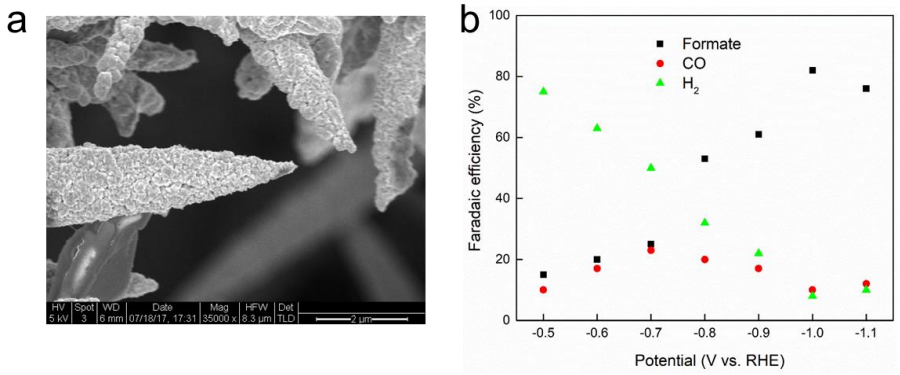

Figure S19. (a) SEM image of uniformly deposited Sn nanoparticles on Au needles by sputtering process. (b) Faradaic efficiency of formate, CO, and H_2 on sputtering Sn on Au needles. We synthesized a thin layer of Sn film on Au needles by sputtering as a control (Figure 19a). The CO_2 reduction activity of sputtering Sn on Au needles was carried out in CO_2 saturated 0.1 M $KHCO_3$. We also calculated the Faradic efficiency of formate for sputtering Sn(S) on Au needles. The Faradaic efficiency of formate on sputtering Sn/Au approached 80% at -1.0 V vs. RHE, which is 300 mV higher than that of Sn(S)/Au (Figure 19b). This agrees well with the qualitative trend from DFT calculation that the presence of sulfur in tin is more favourable for formate production than tin alone.

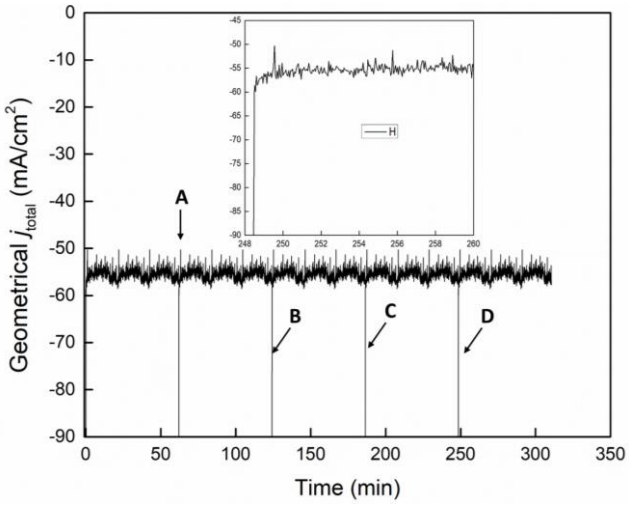

Figure S20. Stability test of Sn(S) cycling between -0.75 V vs. RHE and open circuit potential (Inset is the zoomed part near point D).

Table S1: Optimized Structural Parameters

Material	**a**	**b**	**c**	**α**	**β**	**γ**	**Ref**
Sn	6.42			90			Calc.
Sn	6.46			90			*Nature* 166, 482 (1950)
Sn16S16	4.02	4.43	11.41	90	90	90	Calc.
Sn16S16	4.02	4.44	11.43	90	90	90	*APL Materials*, 2013, 1(1), 011002.
Sn28S4	5.63	5.94	8.07	94.5	83.9	91.1	Calc.
Sn24S8	5.79	5.72	8.04	93.7	81.23	91.1	Calc.
Sn20S12	5.44	6.18	7.58	92.2	93.3	91.1	Calc.

Table S2: Gas phase molecules and their thermodynamic quantities (eV).

Molecule	**E_{DFT}**	**ZPE**	**∫CvdT**	**TS**	**G**
H_2O	-14.21	0.56	0.10	0.67	-14.22
CO_2	-22.95	0.31	0.10	0.66	-22.79
H_2	-6.77	0.27	0.09	0.43	-6.94
CO	-14.78	0.13	0.09	0.67	-15.22
HCOOH	-29.87	0.89	0.11	1.05	-29.71

Table S3: Adsorbate molecules and their thermodynamic quantities (eV).

Adsorbates	E_elec	ZPE	∫CvdT	(-TΔS)	G
$Sn_{16}S_{16}$ (100)					
Slab	-136.18				
CHOO*	-162.40	0.62	0.10	-0.21	-161.89
COOH*	-161.41	0.60	0.12	-0.27	-161.21
CO*	-150.98	0.18	0.18	-0.19	-150.90
H*	-138.53	0.16	0.01	-0.02	-138.38
$Sn_{20}S_{12}$ (100)					
Slab	-128.25				
CHOO*	-153.90	0.61	0.11	-0.26	-153.44
COOH*	-154.01	0.62	0.11	-0.24	-153.78
CO*	-143.29	0.18	0.09	-0.20	-143.22
H*	-131.55	0.16	0.01	-0.01	-131.39
$Sn_{24}S_{8}$ (100)					
Slab	-123.31				
CHOO*	-150.28	0.63	0.09	-0.20	-149.75
COOH*	-149.25	0.63	0.09	-0.18	-148.95
CO*	-149.75	0.18	0.08	-0.17	-138.03
H*	-126.42	0.15	0.01	-0.01	-126.27
$Sn_{28}S_{4}$ (100)					
Slab	-118.41				
CHOO*	-145.29	0.61	0.11	-0.22	-144.80
COOH*	-144.50	0.61	0.11	-0.25	-144.28
CO*	-133.22	0.18	0.08	-0.18	-133.13
H*	-121.44	0.15	0.02	-0.02	-121.29
$Sn_{26}S_{1}$ (111)					
Slab	-98.71				
CHOO*	-125.54	0.61	0.11	-0.23	-125.06
COOH*	-124.42	0.63	0.09	-0.16	-123.86
CO*	-113.49	0.16	0.10	-0.25	-113.48
H*	-101.51	0.14	0.02	-0.03	-101.38
Sn (111)					
Slab	-98.65				
CHOO*	-125.14	0.61	0.11	-0.22	-124.64
COOH*	-124.05	0.62	0.10	-0.20	-123.78
CO*	-112.98	0.17	0.09	-0.21	-112.92
H*	-101.14	0.14	0.02	-0.03	-101.01

Table S4: Theoretical limiting potential (V vs. RHE pH = 0, 273K, 1 atm).

% Sulfur	HCOOH	CO	H_2
0.00	-0.22	-1.08	-1.06
3.8	-0.07	-1.06	-0.75
12.50	-0.11	-0.35	-0.55
25.00	-0.15	-0.58	-0.46
37.50	-1.03	-0.69	-0.28
50.00	-0.51	-1.19	-1.23

Table S5: Calculated Bader partial atomic charges in units of e.

Atom	$Sn_{16}S_{16}$	$Sn_{20}S_{12}$	$Sn_{24}S_8$	$Sn_{28}S_4$	Sn
O1	8.04	7.89	7.96	8.14	8.00
O2	7.97	7.81	7.99	8.14	7.97
Sn1	2.11	4.19	4.23	4.00	3.97
Sn2	1.59	3.53	3.34	4.01	3.95

Table S6: Surface energies for various facets of SnS slab models

Facet	Energy/FU (eV)	Surface Energy (eV)	Relative Surface Energy (eV)
Bulk SnS	-35.47	-	-
100	-35.08	0.20	0.00
110	-34.89	0.29	0.09
111	-34.72	0.38	0.18
211	-34.40	0.54	0.34
311	-34.65	0.41	0.21

Table S7: Surface energies for various facets of SnS slab models.

Facet	Energy/FU	Surface Energy	Relative Surface Energy
Bulk SnS	-35.47	-	-
100	-35.08	0.20	0.00
110	-34.89	0.29	0.09
111	-34.72	0.38	0.18
211	-34.40	0.54	0.34
311	-34.65	0.41	0.21

Table S8. Summary of the electrochemical reduction of CO_2 to formate for homogeneous catalysis.

Catalysts	Potential (V vs. RHE)	Total Current density (mA cm^{-2})	Faradic efficiency of formate	Reference
Sn(S)/Au	-1.05	55	93.9%	Our work
W-containing formate dehydrogenase enzymes	-0.81	0.08	97.3%	Ref[53]
Polymeric$\{Ru^0(bpy)(CO)_2\}_n$	-1	0.05	58%	Ref[54,55]
2,2'-bipyridyl Os complexes	-1.1	0.6	-	Ref[56]
iron carbonyl complex	-0.65	4	95%	Ref[57]
Ir trihydride complex	-1.2	0.45	97%	Ref[58]
Ir dihydride complexes	-1	0.07	95%	Ref[59]
$Iron^0$ Porphyrins	-0.9	0.015	80%	Ref[60,61]

Table S9. Summary of performances for Sn(S)/Au, Sn NPs/Au, and sputtered Sn/Au at -0.6 V and -0.75 V vs. RHE in CO_2 saturated 0.1 M $KHCO_3$ electrolyte.

Samples	Potential (V vs. RHE)	Total geometric current density (mA/cm^2)	Partial current density for formate production (mA/cm^2)	ECSA (cm^2)	ECSA normalized current density for formate production (mA/cm^2)
Sn(S)/Au	-0.6	-34	-32	13.5	-2.4
Sn NPs/Au	-0.6	-26	-4	3.8	-0.9
Sputtered Sn/Au	-0.6	-27	-6	6.9	-0.9
Sn(S)/Au	-0.75	-55	-51	13.5	-3.8
Sn NPs/Au	-0.75	-38	-12	3.8	-3.2
Sputtered Sn/Au	-0.75	-38	-15	6.9	-2.2

Supplemental Experimental Procedures

Energetics Calculations

All density functional theory (DFT) calculations were carried out with the Vienna Ab Initio Simulation package (VASP)[42]. The projector augmented wave (PAW) method[43] was used with the Perdew-Burke-Ernzerhof (PBE)[44] generalized gradient approximation (GGA) exchange correlation functional. All-electron frozen-core PAW pseudopotentials with a plane wave basis set as described by Blöchl[45] were used with a cutoff energy of 500 eV, and fermi smearing width of 0.1 eV and dipole corrections were employed. Monkhorst-Pack mesh[46] was used for k-point sampling with 6x6x6 k-points sampled for the optimization of all bulk structures and 5x5x1 k-points sampled for all vacuum slabs of Sn, S-doped-Sn and SnS. The {100} facet was used with a 4x4x4 atom slab and 20Å between mirror images in the z-axis in the unit cell. Spin polarization was included as it has previously shown to be important for binding energies on metal and metal oxide catalyst surfaces[46]. Structural and unit cell optimizations were performed with the BFGS algorithm until the maximum cutoff was less than 0.02 eV/atom with the structures being fully optimized. Once the slab models were optimized all subsequent thermodynamic calculations were performed with the bottom two layers fixed.

We chose the {100} facet because SnS is a layered metal-sulfide compound and it has been shown that with metal-sulfides the {100} facet is the lowest energy surface[50]. With respect to SnS, experimental studies on atomic layer deposition of tin monosulfide thin films showed that the preferred orientation of SnS upon deposition is when the layer planes are perpendicular to the substrate surface, which is consistent with our model. We have calculated the surface energies for the {100}, {110}, {111}, {211}, and {311} facets of SnS as shown in Table S6. It was found that the {100} facet has the lowest surface energy and is thus expected to be the most stable surface. The surface energies were calculated by the equation, $E_{Surface} = (E_{slab} - E_{bulk})/2$, where E_{slab} is the energy per formula unit of the slab, E_{bulk} is the bulk energy for SnS and this is number is divided by two to account for the top and bottom surfaces in the slab model.

For the calculation of all thermodynamic quantities, the open-source atomic simulation environment (ASE) code[47] was used. The Gibbs free energies were calculated at 298K and 1 atm as outlined below:

$$G = H - TS = E_{DFT} + E_{ZPE} + \int_0^{298} C_v dT - TS$$

where E_{DFT} is the DFT calculated electronic energy, E_{ZPE} is the zero-point vibrational energy, $\int_0^{298} C_v dT$ is the heat capacity, T is the temperature, and S is the entropy. Gas phase molecules such as CO_2 and H_2 were treated using the ideal gas approximation while adsorbates were treated using a harmonic approximation. The DFT calculated energy for gas

phase CO_2 and HCOOH was corrected by 0.45 eV and 0.20 eV respectively commonly employed to account for systematic errors by DFT[48]. Further, the free energies of COOH* were corrected by -0.25 eV as estimation for the hydrogen bond stabilization by water species in solution[24]. The computational hydrogen electrode model (CHE)[49] was used to calculate the change in Gibbs free energy, ΔG, between reaction steps of the CO_2 to HCOOH.

The reactions step for the electrochemical reduction of CO_2 to formic acid, CO, and the competing HER are as follows:

Formic Acid:

$$CO_2 + H^+(aq) + e^- + * \rightarrow HCOO* \quad (1)$$

$$HCOO* + H^+(aq) + e^- \rightarrow HCOOH \quad (2)$$

Carbon monoxide:

$$CO_2 + H^+(aq) + e^- + * \rightarrow COOH* \quad (3)$$

$$COOH* + H^+(aq) + e^- \rightarrow HCOOH \quad (4)$$

$$COOH* + H^+(aq) + e^- \rightarrow CO* + H_2O \quad (5)$$

$$CO* \rightarrow CO + * \quad (6)$$

Hydrogen:

$$H^+ + e^- + * \rightarrow H* \quad (7)$$

$$H* + H^+ + e^- \rightarrow H_2 \quad (8)$$

where * represents either a vacant surface catalytic active site, or intermediate species adsorbed on the active site. The Gibbs energy of formation for an intermediate (ΔG_f) for formic acid is based off reaction 1 ($\Delta G_{formation\ (HCOO*)} = G_{HCOO*} - (G_{CO2} + \frac{1}{2}G_{H2} + G_{slab} - 0.25\ eV)$, for carbon monoxide is based off reaction 3 ($\Delta G_{formation\ (CO*)} = G_{COOH*} - (G_{CO2} + \frac{1}{2}G_{H2} + G_{slab})$), and for hydrogen is based off reaction 4 ($\Delta G_{formation\ (HCOO*)} = G_{H*} - (\frac{1}{2}G_{H2} + G_{slab})$.

To test the effect of different configurations of the Sn to S doping, we performed calculations on three additional configurations. We calculated the formate intermediate binding energy to the surface of all systems including different configurations of the $Sn_{28}S_4$ (12.5% S) slab as shown in Figure S6. The first configuration (the one used in the main text) has the sulfur atoms in the top two layers of the slab surface to appropriately capture the effects of surface embedded sulfur. The second configuration has the in the subsurface layer surrounded by a more well ordered crystalline Sn phase. The third configuration has the sulfur randomly dispersed throughout the entire slab and its optimized structure is much more amorphous. The fourth configuration has sulfur both in on the surface layer and three atom layers deep. It was found that the binding energy of HCOO* remained negative for all slab configurations. While configurations 2 to 4 were slightly more positive than configuration 1, they were all still lower in energy (and thus more favoured) than pure Sn, SnS, or $Sn_{20}S_{12}$ slabs. We also find that that the most positive binding energy found for these configurations was the amorphous and high energy surface of configuration 3.

We have provided the full reaction energy diagram for the reduction of CO_2 to formate (Figure S7). Incorporation of tin sulfide in the $Sn_{28}S_4$ configuration results in the first proton-coupled electron transfer step of CO_2 to adsorbed formate intermediate to be thermodynamically favoured by 0.17 eV. The rate limiting step is now the second proton-coupled electron transfer to the HCOO* intermediate and desorption from surface to form formic acid. Interestingly, the rate limiting step is primarily the initial proton-coupled electron transfer to form the formate intermediate. The calculations now suggest that incorporation of sulfur in the tin lattice lowers the thermodynamic energy barrier for the first proton-coupled electron transfer. In this derivation, we assume that the surface coverage of the CO_2 intermediate is small relative to the total number of active sites on the Sn(S)/Au catalyst.

Bader partial atomic charges were calculated using an open-source code. The volume slice of the electronic charge densities was visualized in Visual Molecular Dynamics (VMD) directly from the VASP CHGCAR file. It was found that the oxygen atoms of the bound formate intermediate on slightly doped Sn(S) structures had slightly higher charge distribution (8.14e) than on tin sulfide (8.04e) or pure tin (8.0e) (Table S5). Thus, the electron density of the bound oxygen atoms is slightly higher on slightly doped Sn(S) suggesting a stronger Sn-O intermediate bond.

The atomic surface area was calculated via the Connolly accessible surface area calculation as implemented in Materials Studio. This method was first developed to calculated the solvent accessible surface area for proteins and nucleic acids[51], but has since been used in materials science of porous materials such as metal organic frameworks[52]. Simply, this is a method which can calculate a smooth three-dimensional contour based on a rolling-probe of certain size. The Connolly accessible surface areas were calculated using a Connolly radius of 1.4 Å and a grid interval of 0.75 Å.

Materials and Methods

Chemicals

The tin precursor, tetrakis(dimethylamino)-tin(IV) (TDMASn, 99.99%-Sn) was purchased from Strem Chemicals. $HAuCl_4$ (99.99%), Sn nanoparticles with average 10 nm and commercial SnS were purchased from Sigma-Aldrich.

Synthesis of SnS_x on Au needles

Au needles were prepared on carbon paper (Toray TGP-H-060, purchased from Fuel Cell Store) through an electrodeposition process as previously reported[3]. The Au needle electrode was formed using a 160 mM $HAuCl_4$ and 0.5 mol/L solution, and direct current potential amperometry at −400 mV for 300 s. Au nanoneedle morphology provides the enhancement to the current density due to field-induced regent concentration effect.
SnS_x was deposited at 90 ^oC using tetrakis(dimethylamino)-tin(IV) (TDMASn, 99.99%-Sn, Strem Chemicals INC) and H_2S at a constant growth rate of 0.035 nm per cycle measured by ellipsometry. TDMASn was held at 65 ^oC. Nitrogen was used as a carrier gas (99.9999% pure, Carbagas) with a flow rate of 10 sccm[38].

Synthesis of Sn nanoparticles on Au needles

Electrophoretic deposition was implemented to uniformly deposit Sn nanoparticles on nano-structured Au electrode[39, 40]. Specially, 10 mg/L Sn nanoparticles in ethanol was placed in the ultrasonic bath for 50 min and centrifuged for 30 min at 4,000 RPM to remove large nanoparticles from the suspension. Finally, a DC power supply of 20 V was applied for 20 min to deposit Sn nanoparticles.

Characterization

High resolution TEM (HRTEM) images were taken on an FEI monochromated F20 UT Tecnai microscope operated at 200 kV. Scanning transmission electron microscopy (STEM) elemental mapping of samples were taken on a FEI Titan 80-300 environmental (scanning) electron microscope (E(S)TEM), a spot size of 6 with a C2 aperture size of 70 um. The samples were prepared by dropping catalyst powder dispersed in ethanol onto carbon-coated copper TEM grids (Ted Pella, Redding, CA) using micropipettes and were dried under ambient conditions. Scanning electron microscope (SEM) were acquired using a Hitachi SU8230 scanning electron microscope operated at 1.0 kV. Powder X-ray diffraction (XRD) patterns were obtained with MiniFlex600 instrument. Data were collected in Bragg-Brentano mode using 0.02° divergence with a scan rate of 0.1° s^{-1}. X-ray photoelectron spectroscopy (XPS) measurements were carried out in a Thermo Scientific K-Alpha system, with a 300 μm spot size, 75 eV pass energy, and energy steps of 0.05 eV, aluminum anode X-ray excitation. The Shirley algorithm was used to fit the background. Then the atomic ratio is computed by summing over the curves over the background and taking into account the absorption cross-section of Sn and S to determine relative ratios from their intensities (Figure S10). The in-situ spectroelectrochemical (ATR-FTIR) measurements were performed on a Bruker IFS 66/S Spectrometer. For the in-situ technique, a sealed electrochemical cell (Figure S18) with Pt as counter electrode, Sn(S) as working electrode and Ag/AgCl reference electrode was mounted in the spectrometer. The system was continuously flushed with CO_2 saturated 0.1 M $KHCO_3$. Sn(S) was deposited onto a Germanium crystal (1x1x0.2 cm parallelepiped, angle 45°C) as reflection element. During the spectroscopic recording, a constant potential was applied (-0.3 V, -0.5 V, and -0.7 V vs. RHE, respectively) (Figure S18).

X-ray absorption measurement

The Sn K-edge spectra were collected at the 06ID-1 Hard X-ray MicroAnalysis (HXMA) beamline from Canadian Light Source. *In situ* Sn L_3-edge and S K-edge spectra were collected at the soft X-ray Microcharacterization (SXMRB) beamline from Canadian Light Source. For every edge, the scanning time was 30 s and repeated for ten times, and the fluorescence of every edge was collected at the same absorption edge. The partial fluorescence yield (PFY) was extracted from all SDDs by summation of the corresponding metal L emission lines. *Ex situ* Sn L_3-edge spectra were collected at Beamline 10.3.2 from the Advanced Light Source. The X-ray wavelength was monochromatized by a Si(111) double-crystal, fixed exit monochromator. The intensity of the incident X-ray radiation, I_0, was monitored with a nitrogen filled ionization chamber. All data were collected in fluorescence mode with a 7-element Ge detector (Canberra). All spectra were aligned according to a glitch in I_0 near the absorption edge.

Electrochemical Measurements

Electrochemical measurements were performed using a three-electrode system connected to an electrochemical workstation (Autolab PGSTAT302N) with built-in electrochemical impedance spectroscopy (EIS) analyzer. All CO_2 reduction experiments were performed using a three-electrode system connected to an electrochemical workstation (Autolab PGSTAT302N). Ag/AgCl (with saturated KCl as the filling solution) and platinum mesh were used as reference and counter electrodes, respectively. Electrode potentials were converted to the reversible hydrogen electrode (RHE) reference scale using E(RHE) = E(Ag/AgCl) + 0.197 V+0.0591×pH. The calibrations of Ag/AgCl reference electrode and Ag wire reference electrode were conducted in the standard three-electrode system (the same system as that for performance measurements) as reference electrodes, using Pt foil as working and counter electrodes.

The electrolyte was 0.1 M $KHCO_3$ saturated with CO_2. Formate was quantified on GC with a mass spectrometry (PerkinElmer Clarus 600 GC-MS System). Assuming that two electrons are needed to produce one formate molecule, the Faradaic efficiency was calculated as follows:

Faradaic efficiency=$2F\times n_{formate}/Q=2F\times n_{formate}/(I\times t)$, where F is the faraday constant, I is the current, t is the running time and $n_{formate}$ is the total amount of produced formate (in moles).

Electrochemically active surface area

To evaluate the effect of surface area, we measured the electrochemically active surface area (ECSA) for Sn(S)/Au and Sn NPs/Au from the electrochemical double-layer capacitance of the catalytic surface[26-29]. The electrochemical capacitance was determined by measuring the non-Faradaic capacitive current associated with double-layer charging from the scan-rate dependence of cyclic voltammograms (CVs) (Figure S8)[28,29]. The double-layer charging current is equal to the product of the scan rate, v, and the electrochemical double-layer capacitance, C_{DL}, as given by the equation 1.

$$i_c = v\, C_{DL} \qquad (1)$$

Thus, a plot of i_c as a function of v yields a straight line with a slope equal to C_{DL} (Figure S8b and Figure S8d). We then concluded that the ECSA of Sn(S)/Au electrode is three times higher than Sn NPs/Au electrode.

The specific ECSA of the electrodes is calculated from the double layer capacitance according to equation 2:

$$ECSA = C_{DL}/C_s \qquad (2)$$

where C_s is the specific capacitance of the sample or the capacitance of an atomically smooth planar surface of the material per unit area under identical electrolyte conditions. For our estimates of surface area, we use general specific capacitances of C_s = 0.029 mF based on typical reported values[29,30].

From ECSA normalized performance of CO_2 reduction to formate, the high catalytic activity of Sn(S)/Au includes an appreciable intrinsic (not surface-area-related) contribution (Figure S9).

iR correction

We carried out iR correction to further lower the overpotential for formate production[28,62]. Specifically, the solution resistance was determined by electrochemical impedance spectroscopy ((Figure S16) R_s=45Ω for Sn NPs/Sn foil, Sn(S)/Sn foil and R_s=33Ω for Sn NPs/Au, Sn(S)/Au, respectively). At all potentials tested, the potential was manually corrected

using Ohm's law:

$$E=E_{app}-iR_s*0.85 \text{ (compensating for 85\% of the resistance)}$$

where R_s represents the calculated solution resistance, i is the measured current, and E_{app} is the applied potential on the working electrode.

Supplemental References

42. Hafner J. (2008). Ab-initio simulations of materials using VASP: Density-functional theory and beyond. *J Comput Chem* **29**(13)**:** 2044-2078.

43. Blöchl PE. (1994). Projector augmented-wave method. *Phys. Rev. B* **50**(24)**:** 17953-17979.

44. Ernzerhof M, Scuseria GE. (1999). Assessment of the Perdew–Burke–Ernzerhof exchange-correlation functional. *J. Chem. Phys.* **110**(11)**:** 5029-5036.

45. Kresse G, Joubert D. (1999). From ultrasoft pseudopotentials to the projector augmented-wave method. *Phys. Rev. B* **59**(3)**:** 1758-1775.

46. Monkhorst HJ, Pack JD. (1976). Special points for Brillouin-zone integrations. *Phys. Rev. B* **13**(12)**:** 5188-5192.

47. Hansen HA, Varley JB, Peterson AA, Norskov JK. (2013). Understanding Trends in the Electrocatalytic Activity of Metals and Enzymes for CO_2 Reduction to CO. *J Phys. Chem. Lett*, **4**(3)**:** 388-392.

48. Bahn S, Jacobsen K. (2002) An object-oriented scripting interface to a legacy electronic structure code. *Comput. Sci. Eng.* **4**(3)**:** 56-62.

49. Peterson AA, Pedersen A, Studt F, Rossmeisl J, Nørskov J. (2010). How copper catalyzes the electroreduction of carbon dioxide into hydrocarbon fuels. *Energy. Environ. Sci.* **3**,116-122.

50. Zhang L, Song Q, Zhang SB. (2010). Exceptionally strong hydrogen bonds affect the surface energy of colloidal nanocrystals: methylamine and water adsorption on PbS. *Phys. Rev. Lett.* **104**(11)**:** 116101.

51. Connolly ML. (1983). Solvent-Accessible Surfaces of Proteins and Nucleic-Acids. *Science* **221**(4612)**:** 709-713.

52. Nandi; S, Luna; PD, Daff; TD, Rother; J, Vaidhyanathan R. A (2015). single-ligand ultra-microporous MOF for precombustion CO_2 capture and hydrogen purification. *Science Advances* **1**(11)**:** 1-9.

53. Reda T, Plugge CM, Abram NJ, Hirst J. (2008) Reversible interconversion of carbon dioxide and formate by an electroactive enzyme. *Proc. Natl. Acad. Sci. USA* **105**(31)**:** 10654-10658.

54. Noblat J, Noelle N, Deronzier A, Ziessel R, Zsoldos D. (1994) Formation of Polymeric {Ruo(bpy)(CO)} Films by Electrochemical Reduction of [Ru(bpy) (CO)z]$(PF_6)_2$: Its Implication in CO_2 Electrocatalytic Reduction. *Inorg. Chem.* **33**(2)**:** 4410-4412.

55. Ishida H, Tanaka K, Tanaka T. (1987). Electrochemical CO_2 Reduction Catalyzed by [R (bpy) (C0)]$^+$ and [Ru(bpy)(CO)Cl]$^+$. The Effect of pH on the Formation of CO and HCOO-. *Organometallics* **6**(4)**:** 181-186.

56. Bruce M, Megehee E, Vaidhyanathan R. (1992). Electrocatalytic Reduction of Carbon Dioxide Based on 2,2'-Bipyridyl Complexes of Osmium. *Inorg Chem* **31**(12)**:** 4864-4873.

57. Taheri A, Thompson EJ, Fettinger JC, Berben LA. (2015). An Iron Electrocatalyst for Selective Reduction of $CO_2$to Formate in Water: Including Thermochemical Insights. *ACS Catal.* **5**(12)**:** 7140-7151.

58. Ahn ST, Bielinski EA, Lane EM, Chen Y, Bernskoetter WH, Hazari N*, et al.* (2015). Enhanced CO_2 electroreduction efficiency through secondary coordination effects on a pincer iridium catalyst. *Chem. Commun (Camb)* **51**(27)**:** 5947-5950.

59. Kang P, Cheng C, Chen Z, Schauer CK, Meyer TJ, Brookhart M. (2012). Selective electrocatalytic reduction of CO_2 to formate by water-stable iridium dihydride pincer complexes. *J. Am. Chem. Soc.* **134**(12)**:** 5500-5503.

60. Hammouche M, Lexa D, Momentea M, Sav6an J. (1991). Chemical Catalysis of Electrochemical Reactions. Homogeneous Catalysis of the Electrochemical Reduction of Carbon Dioxide by Iron("0") Porphyrins. Role of the Addition of Magnesium Cations. *J. Am. Chem. Soc.* **113**(8)**:** 8455-8466.

61. Appel AM, Bercaw JE, Bocarsly AB, Dobbek H, DuBois DL, Dupuis M*, et al.* (2013). Frontiers, opportunities, and challenges in biochemical and chemical catalysis of CO_2 fixation. *Chem. Rev.* **113**(8)**:** 6621-6658.

62. Li, Y., Cui, F., Ross, M. B., Kim, D., Sun, Y., & Yang, P. (2017). Structure-Sensitive CO_2 Electroreduction to Hydrocarbons on Ultrathin 5-fold Twinned Copper Nanowires. *Nano. Lett*, 17(2), 1312-1317.